

Long Term Project Report : Interim/Final

Summary Page

1. Beamtime Used

Please give a short summary of progress for each scheduling period for which beamtime has been allocated/used :

Scheduling period	Beamline(s) Used	Shifts Used	Summary of results obtained
2013 /II	ID19	12	<p>Technical</p> <ul style="list-style-type: none"> - Implementation of PCO DIMAX camera and ultra fast tomography in 0.2s with optics of 1.1μm realized. - First implementation of python code for live control (fast 2D slice reconstruction) - First implementation of 2D strain correlation in live - Multi-resolution with one camera which changes in less than 15s. <p>Scientific application</p> <ul style="list-style-type: none"> - Ultra fast tomography on the solidification of Al-Si-Fe alloys : intermetallics nucleation as a function of composition in Fe - Preliminary experiments on liquid foams with fibers.
2014 /I	ID19	6	<p>Technical :</p> <ul style="list-style-type: none"> - New algorithm for low number of projections reconstruction giving interesting results with 200 projections only : one of them has been implemented in PyHST2 - Development of users friendly macros for the configuration of PCO DIMAX camera for fast tomography. <p>Scientific application :</p> <ul style="list-style-type: none"> - Study of nucleation and growth of intermetallics in Al-Si-Fe alloys. Ultra fast scans in 0.2 seconds have been done : we show that thermodynamic calculation are not respected at high level of Fe because it does not take into account undercooling effect. - Indentation of liquid foams : it was possible, for the first time, to obtain qualitative information about the behaviour of crystalline ordering in micro-foams under indentation. - Phase separation glass : 4D experiments with scan time between 1 – 2 seconds allowed to establish the

			hydrodynamics behavior of phase separation glass during isothermal treatment.
2014 /II	ID19	18	<p>Technical :</p> <ul style="list-style-type: none"> - Development of the high temperature furnace under controlled atmosphere using slip rings for fluids. - Simplification and merging of fasttomo macros to have only one version whatever the detector used (PCO DIMAX, PCO Edge, FReLoN). - Definition of triple mic optics with Optique Peter for fast multiresolution with one camera : this device is financed by LTP partners. <p>Scientific application :</p> <ul style="list-style-type: none"> - Glass formation was for the first time investigated with 4D tomography under CO2 atmosphere. - Intrumescent coatings : it was possible for the first time and with very fast acquisition (0.15 seconds per scan) to study in 4D the foaming of several intrumescent coatings. - Damage in new generation of composites : it was possible to identify with in situ tomography the main mechanisms (nucleation, growth and coalescence of damage) as a function of matrix and volume fraction of metallic glass reinforcements
2015 /I	ID19	3	<p>Technical :</p> <ul style="list-style-type: none"> • Improvement of the specific user friendly macros for fast in situ acquisition with PCO DIMAX camera • Liveslice development and test • Final validation of a high temperature induction furnace with vacuum or gas for fast in situ experiments (SVI) • Multi-resolution reconstruction using low resolution data set <p>Scientific application :</p> <ul style="list-style-type: none"> • solidification of Al-Mg-Si alloys : interaction of nanoparticles with solidification front in new generation of nano-composites. • Aqueous protein foam samples : in situ growth of pores using multiresolution tomography • Glass formation : Nucleation and growth of bubbles in molten silicate glass and effect of sulfur. • Ductile metals and composites : damage quantification (decohesion/rupture of particles) versus strain and comparison to numerical simulation <p>Benefit for other users : several industrial and academic experiments have used the development of this LTP (see list below)</p>

2015 /II	ID19	18	<p>Technical</p> <ul style="list-style-type: none"> • Final validation of the routine fasttomo_awerner in several configuration of scan acquisition. • Finalization with Optique Peter about the acquisition of a triple objective white beam optics for single camera fast multi resolution. • Test of a new concept of high temperature compression/tension device • Design of a new room temperature tensile device for fast acquisition <p>Scientific application :</p> <ul style="list-style-type: none"> • Glass formation : Reactivity of glass batch materials at high temperature. kinetics and geometry of chemical reactions between powders of glass raw materials (quartz sand, sodium and calcium carbonate) using controlled atmosphere furnace • Intrumescent coatings : real time observation and 3D quantification as well as modelling of the dynamic foaming process including coating expansion and internal structure evolution as a function of heating rate • Ductile metals and composites : void nucleation, growth and coalescence process in 6XXX alloys. The key element setting the fracture strain is the effect of particle size distribution and spatial distribution on the void nucleation and coalescence processes. • Amorphous bulk metallic composites : co-deformation of composites with well controlled temperature : effect of bulk metallic particles volume fraction and strain rate. • Benefit for other users : several industrial and academic experiments have used the development of this LTP (see list below)
2016 /I	ID19	6	<p>Scientific application : high temperature deformation of amorphous metal composites</p>

2. Resources Provided by User team (financial, personnel, technical...):

Staff :

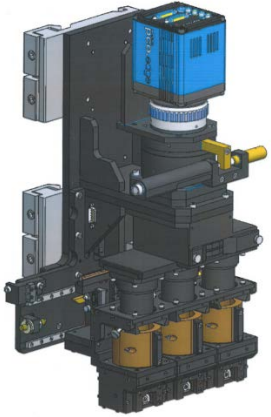
- January 2014 – December 2014 : one post doc : Rémi Daudin (SIMAP) based at 60% at ESRF
- January 2014 – December 2014: two researchers Pierre Lhuissier (10%), Luc Salvo (5%) (SIMAP) on the LTP
- January 2014 – December 2014: Two technicians Franck Peloux et Xavier Bataillon (SIMAP): 2 weeks
- November 2014 – December 2014 : 1 year engineer (Werner Augustin) recruited based 100% at ESRF (payment 50% SIMAP/ 50% ESRF)
- January 2015 – september 2015 : one post doc : Rémi Daudin (SIMAP) based at 60% at ESRF
- october 2015 – december 2015 : one post doc : Rémi Daudin (SIMAP) working 25% for LTP.
- October 2015 – october 2016 : Thérèse Bormann (SIMAP) working 100% on high temperature tensile / compression device and high temperature of amorphous composites.
- January 2016 – February 2016: two researchers Pierre Lhuissier (10%), Luc Salvo (5%) (SIMAP) on the LTP
- January 2016 – February 2016: Two technicians Franck Peloux et Xavier Bataillon (SIMAP): 1 month on high temperature tensile / compression device

Technical : Modification of a high temperature induction furnace with vacuum or gas for fast in situ experiments (SVI) :

- Improvement of the specific user friendly macros for fast in situ acquisition with PCO DIMAX camera and fast reconstruction
- Discussion with Optique Peter about the acquisition of a triple objective white beam optics for single camera fast multi resolution.
- Development of multi-resolution using two PCO cameras at the same time.
- Improvement of the specific user friendly macros for fast in situ acquisition with PCO DIMAX camera
- Liveslice development and test
- Final validation of a high temperature induction furnace with vacuum or gas for fast in situ experiments (SVI) :
- Final validation of the routine fasttomo_awerner in several configuration of scan acquisition.
- Finalization with Optique Peter about the acquisition of a triple objective white beam optics for single camera fast multi resolution.
- Test of a new concept of high temperature compression/tension device
- Design of a new room temperature tensile device for fast acquisition
- Multi-resolution reconstruction using low resolution data set

Financial and benefit for users and industry :

- The partners of the LTP finance a new triple optic developed by Optic Peter. This is a unique device available in the world on synchrotron which will give ID19 a very large versatility and easy operation at spatial resolution between 0.5µm and 2µm with changes in less than few seconds. This opens the possibility to perform fast multi-resolution tomography

	<p>Triple mic develop by Optic Peter and financed by partners</p> <ul style="list-style-type: none"> ▪ MATEIS/GISMA : 30000 euros. ▪ SIMAP/GISMA : 30000 euros ▪ SVI : 10000 euros ▪ NOVITOM : 8000 euros ▪ Univ Wuerzburg : 8000 euros
---	---

- Moreover the development performed in this LTP benefits to lot of academic users via proposal but also allow to obtain industrial shifts : below you will find the list of scientific experiments (MA,ME,LS,MD,EGV) as well as industrial experiments (IN) that directly benefit from the LTP work according to each period

2014-I	2015-II
MA-2190	LS-2426
MA-1498	MA-2758
	MA-2774
2014-II	2016-I
MA-2405	MA-2984
LS-2354	MA-2989
	MA-2994
	MD-957
	IN-955
	ES-410
	IN-585
	IN-982
2015-I	2016-II
IN-832	IN-662
IN-832	IN-964
EV-135	MA-2994
LS-2343	MA-3234
MA-2574	ME-1425
IN-708	

- **In situ sample environment : new sample environment are available for ESRF users**
 - MATEIS 30000 euros : new room temperature tensile/compression device for fast tomography
 - SVI : 1500 euros investment in the development of a rotary joint for the high temperature furnace
 - SIMAP : 5000 euros : development of the new high temperature compression device for ultra-fast tomography.

3. **Technical and Scientific Milestones Achieved** (in relation to the milestones identified in the original proposal).

The technical and scientific milestones achieved are presented according to the tasks that were originally defined in the LTP. Tasks are described in details below but it can be summarized below. During this LTP partners worked both on the scientific cases, published and presented widely in the community, and on the development of ultra-fast in situ tomography and user friendly routines for acquisition and reconstruction. This work already benefits to a lot of users and industry (as shown in the previous table) and surely will continue to be beneficial to academic users as well as industrial users in the future. These technical developments were possible thanks to large human resources that partners put on the beamline and outside of the beamline but also with a very fruitful collaboration with ESRF staff. Partners also financed a unique optic in the world for ultrafast tomography (86 000 euros) which will allow multi-resolution ultra-fast tomography. Therefore we really think that this LTP is a success with a good trade off between development and science.

Task 1 : Technical development

Task 1.1 : data acquisition

Data acquisition and control : R. Daudin, P.Lhuissier (SIMAP) and ESRF staff.

Several new acquisition menus have been developed on the ID19 beamline for experiments using the PCO-Dimax camera. These menus were created to help users setting up their acquisition in accordance with the experimental needs. It is thus now possible to easily tune the experiment parameters that basically consist in 3 different modes

- **Static scans:** only one scan,
- **Multiple acquisitions:** series of successive scans with elapse time between each scans (for downloading data or record longer time),
- **Continuous acquisition:** recording all projections continuously over several turn (for best temporal resolution)
- **Multiple continuous acquisition:** series of successive continuous acquisition with elapse time between each one.

The different acquisition modes can be selected by changing different parameters (*tomo_loop*, *nbtomo*, etc...) in the main menu (*pcotomoconfig* and *proctomoscanconfig*). A convenient way to

switch from one mode to another is to define specific sub-function (see Figure 1) at the demand of the users to quickly skip from one protocol to another. This is now a routine on ID19 and it really helps non expert users to easily perform their experiment without worrying about the acquisition parameters.

<pre>def single_scan '{ pcotomoconfig latency_time 5e-05 pcotomoconfig save_data 1 pcotomoconfig scan_dir nice pcotomoconfig sino_dir nice pcotomoscanconfig lab_name simap pcotomoscanconfig esrf_exp_number in832 pcotomoscanconfig roi_y 816 pcotomoscanconfig roi_x 816 pcotomoscanconfig tomo_loop 1 pcotomoscanconfig waiting_turns 0 pcotomoscanconfig download_scans 1 pcotomoscanconfig flat_after 1 pcotomoscanconfig dark_after 1 pcotomoscanconfig flat_before 0 pcotomoscanconfig dark_before 0 pcotomoscanconfig nproj 800 pcotomoscanconfig nbtomo 1 pcotomoscanconfig radio_exp_time 0.001 pcotomoscanconfig start_angle 90 pcotomoconfig start_turn 5 runpcotomoSIMAP "\$1" }'</pre>	<pre>def continuous '{ pcotomoconfig latency_time 5e-05 pcotomoconfig save_data 1 pcotomoconfig scan_dir nice pcotomoconfig sino_dir nice pcotomoscanconfig lab_name simap pcotomoscanconfig esrf_exp_number in832 pcotomoscanconfig roi_y 720 pcotomoscanconfig roi_x 1008 pcotomoscanconfig tomo_loop 1 pcotomoscanconfig waiting_turns 0 pcotomoscanconfig download_scans 1 pcotomoscanconfig flat_after 0 pcotomoscanconfig dark_after 0 pcotomoscanconfig flat_before 1 pcotomoscanconfig dark_before 1 pcotomoscanconfig nproj 800 pcotomoscanconfig nbtomo 50 pcotomoscanconfig radio_exp_time 0.001 pcotomoscanconfig start_angle 90 pcotomoconfig start_turn 5 runpcotomoSIMAP "\$1" }'</pre>	<pre>def multiple '{ pcotomoconfig latency_time 5e-05 pcotomoconfig save_data 1 pcotomoconfig scan_dir nice pcotomoconfig sino_dir nice pcotomoscanconfig lab_name simap pcotomoscanconfig esrf_exp_number in832 pcotomoscanconfig roi_y 720 pcotomoscanconfig roi_x 1008 pcotomoscanconfig tomo_loop 50 pcotomoscanconfig waiting_turns 4 pcotomoscanconfig download_scans 1 pcotomoscanconfig flat_after 0 pcotomoscanconfig dark_after 0 pcotomoscanconfig flat_before 1 pcotomoscanconfig dark_before 1 pcotomoscanconfig nproj 800 pcotomoscanconfig nbtomo 1 pcotomoscanconfig radio_exp_time 0.001 pcotomoscanconfig start_angle 90 pcotomoconfig start_turn 5 runpcotomoSIMAP "\$1" }'</pre>
--	--	--

Figure 1: Examples of different sets of acquisition parameters used for different acquisition protocols.

The decision concerning the acquisition strategy is mainly driven by the limited internal memory of the camera. A new Excel sheet (Figure 2) is now available for users to help them defining the best acquisition conditions for their experiment. As in situ experiments are always based on making concessions between spatial and temporal resolution, this gives instant information on what a user can hope to get in the different conditions.

B	C	D	E	F	G	H	I	J	K	L	
Limited memory in the camera (GB):			48.0	Estimated Transfer Rate = f (size) (Mb/s)			215				
SCAN PARAMETERS						SCAN PROPERTIES					
Roi_x (pix)	Roi_y (pix)	Number of projections	Exposure time (s)	Pixel size (µm)	Transfer rate (MB/s)	Time scan (s)	Field of view (mm)	Size of one scan (GB)	Rei	st	
1536	2016	1500	0.005	1.1	190	7.5	1,69 x 2,22	8.653			
Comments on transfer rate:			Comment 1: Transfer rate is not constant. It ranges between 70 MB/s to 170 MB/s depending on the traffic. You can use these low and high values to prepare you				Comment 2: Incompressible time for dialogue bet camera and the device server is necessary in th protocole. Hence, very small files are not very fast transfer time is negligible compared to dialogi				
3 POSSIBLE MODES											
CONTINUOUS ACQUISITION : Consecutive scans all recorded in the camera memory (best time resolution)											
Maximum number of scans			Total time recorded			Time to download the film					
4			30 (s) or 0,5 (min)			258 (s) or 4,31 (min)					
LIMITED MULTIPLE ACQUISITION : Pause between scan, all recorded in the camera memory (to record longer times)											
Maximum number of scans		Waiting turns (choosen)	One scan every	During		Time to download all scans					
4		5	90 (s)	360 (s) or 6 (min)		258 (s) or 4,31 (min)					
IT IS WORTH DOWNLOADING DATA BETWEEN SCANS											
UNLIMITED MULTIPLE ACQUISITION : Pause between scans with download (record forever but worse time resolution)											
Maximum number of scans		Time to download one scan		Recommended waiting turns	One scan every	During					
UNLIMITED		46 (s) or 0,78 (min)		3	60 (s)	Forever					

Figure 2: Illustration of the Excel sheet available for users. Filling the scan parameters and the estimation of the transfer rate automatically computes all information (size of 3D images, recorded time and temporal resolution) in the different acquisition modes.

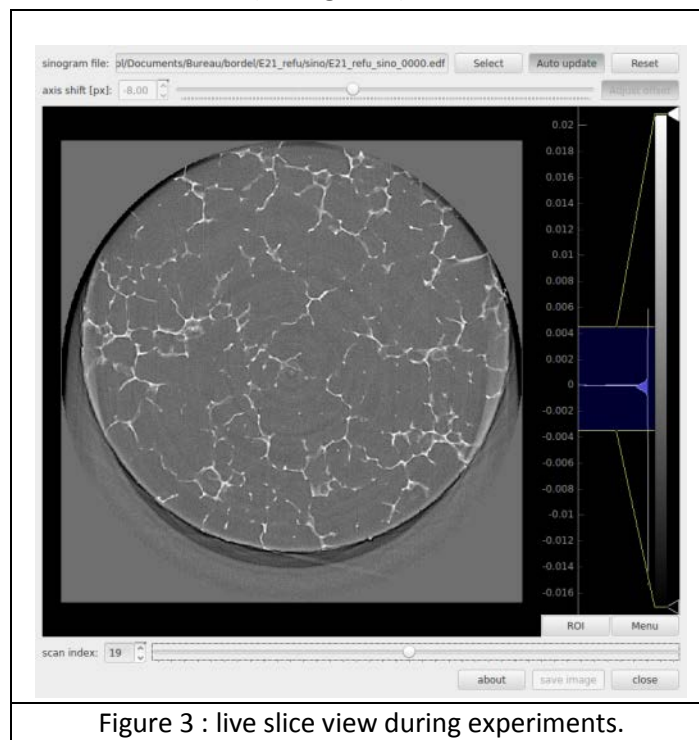
Benefit to ID19 : these developments are very useful to users and consolidate the fact that fast in situ tomography (scan in less than 1 second with 1.1 microns pixel size) can be done routinely now on ID19. Furthermore this works facilitate the local contact work to provide easy use of the acquisition macros. The various mode of acquisition that have been designed cover most of the situation faced by users and the fact that it has been used during 9 industrial and academic experiments during 2015 show clearly the benefit for ID19 and ESRF.

Task 1.1.1 : live control

Live reconstruction and correlation : P.Lhuissier (SIMAP)/J. Dittman (Univ of Wuerzburg) /M. Ullherr (LRM)

A custom GPU-accelerated parallel-beam FBP-reconstruction together with a custom GUI prototype was developed in collaboration with M. Ullherr (LRM) and adopted for use at ID19 by P. Lhuissier. It

enables live reconstruction and display of single slices simultaneous to data acquisition with the prospect of (automated) triggering of full-view imaging protocols based on manual or automatic live image analysis. The Live Slive View consists of three components, namely the actual FBP reconstruction module (jonas.dittmann@physik.uniwuerzburg.de), the image display module [4] and the graphical user interface. It is implemented in Python [1] with the help of PyCUDA [2], PyQt [3] and PyQtgraph [4]. Integration with the beamline was done by P. Lhuissier. The combination of GPU accelerated reconstruction and OpenGL image display allow for repetition rates of 2 Hz even at 2048² resolution, and significantly faster at lower resolutions. Different reconstruction parameters such as axis offset can be adjusted during live preview. The software can easily be extended with automated image analysis functions which may further be used to trigger experimental equipment or acquisition protocols. The live slice viewer was adapted to live acquisition on ID19 and installed on the local buffer system (lbs191). It was made consistent with SPEC acquisition macros (file location and format, flat and dark files...) and the software was modified in order to automatically update the slice as a new scan is recorder and to add it in a stack. It allows the used to easily browser along the time axis while the acquisition is still processing. It provide thus a live view inside the sample with an easy visual capture of minor microstructure evolutions (see figure 3)



Benefit to ID19. Live tomographic view into samples as they are scanned. This can ease beamline setup and calibration and gives immediate feedback on sample condition and image quality to the user. For high-speed acquisitions that have a very limited time window due to limited camera RAM, the live preview facilitates manual or automated triggering of actual high-speed acquisition sequences at the right time point. The main limitation is due to the time transfer between camera and computer (few seconds) but the reconstruction is quite fast. An extension to fast 3D reconstruction and 2D visualization will be tested during next LTP dates.

References.

[1] Python <https://www.python.org/>

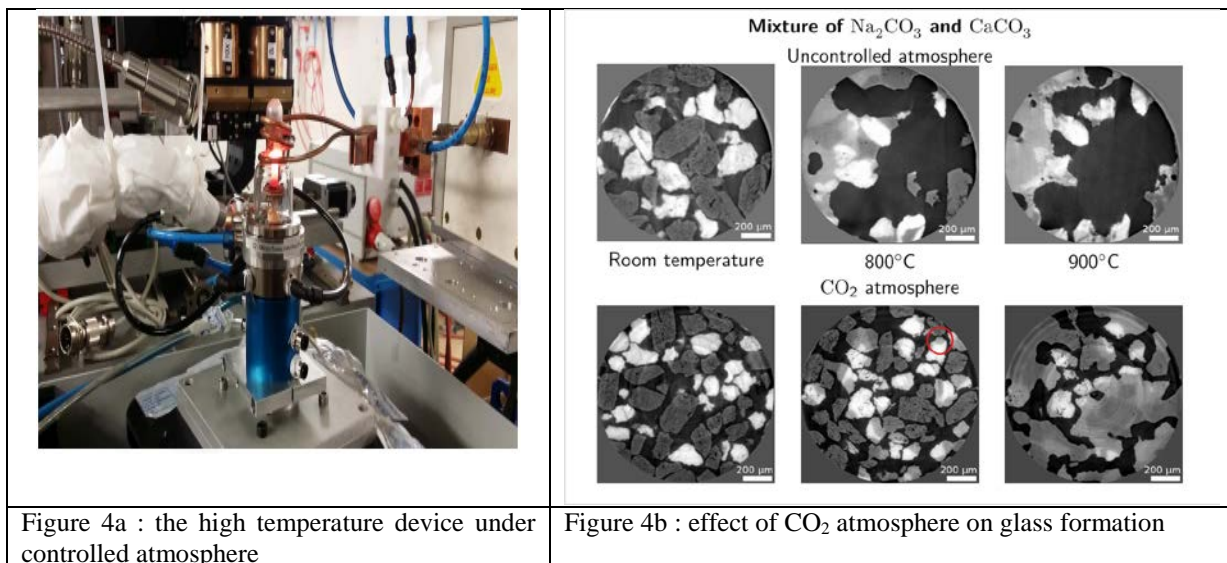
- [2] PyCUDA <https://mathematician.de/software/pycuda/>
- [3] PyQt <https://riverbankcomputing.com/software/pyqt/intro>
- [4] PyQtgraph <http://pyqtgraph.org/>

Task 1.2 : Sample environment

Task 1.2.1 : Heating devices

Modification of a high temperature furnace (controlled atmosphere up to 1600°C) E. Garre, E. Guillard (SVI), E. Boller (ESRF)

To allow continuous rotation of the sample environment furnace with gas environment a rotary joint was bought and adapted by SVI. (figure 4a). The controlled-atmosphere furnace available on ID19 relies on induction heating. For non-conductive materials, a susceptor material must be used to heat the sample. In previous experiments, we used a Molybdenum susceptor with a hole to put the sample in. However, Molybdenum being very absorbing, we could only observe the part of the sample over the susceptor. Therefore, large temperature gradients (~100°/mm at 1000°C) were measured in the sample. For non oxidizing atmosphere, we tested graphite susceptors, that are transparent enough to X-rays so that the sample can be completely inside the susceptor. Using materials of known melting temperature, we could check that the temperature gradient is now much lower (of the order of 20°C/mm). Therefore work is needed to improve the temperature homogeneity within the samples. Figure 4b shows the difference of glass formation with and without CO₂ atmosphere.



Benefit to ID19. Up to now it was not possible to perform high temperature thermal treatment at high temperature (above 1000°C) under controlled atmosphere. Despite the fact that there is a need of more controlled temperature it has been used during industrial shift IN832.

Task 1.2.2: Mechanical devices

Development of room temperature tensile device for fast acquisition : E. Maire/J. Adrien (MATEIS)

During the LTP, Mateis has designed his new tensile rig, able to rotate continuously, and better equilibrated compared to the preceding one. The new machine, shown in figure 5, is lighter and can

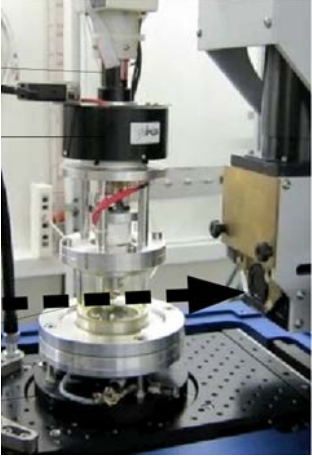
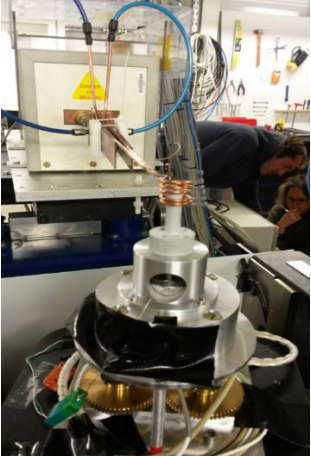
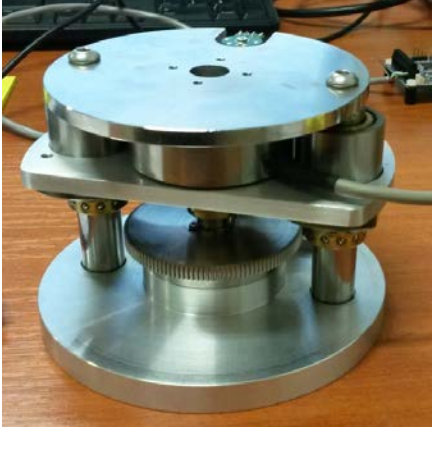
rotate very fast. 10 rotation per second has been achieved outside the synchrotron and the machine was rotating with minor vibration, proving that this could be used at the same speed on the rotation stages of the ESRF. During the LTP, we have used the rig at moderate rotation speed, mostly because the rotation speed at the ESRF are limited. It allowed us to record scans in one seconds (rotation speed 0.5 round per second) and this in turn allowed us to perform continuous in situ tensile experiments. During the LTP, we have frequently compared the results of the continuous mode and of the interrupted mode. It was shown that if the samples are fragile, using the continuous mode could be very helpful. Conversely, high speed is not required when the sample is ductile because interrupted mode can be used.

Development of a high temperature tensile machine : P. Lhuissier (SIMAP) / NOVITOM

Two device have been developed : one for the MR tomograph and one for the HR tomograph based on NOVITOM machine.

- The concept is based on the NOVITOM room temperature device where motor, load cell is underneath the sample which is strained thanks to a bell. The advantages of such a system is that it minimizes the wobbling that is often observe when motors are place above the sample and thanks to the bell it is possible to adapt an induction furnace and even a gas flow. During this session we focused on the modification of the device to allow heating and it worked well. We designed a BN bell which cover the sample that is on a ceramic rod and we used the ESRF sample environment induction furnace with a dedicated coil (see figure 6) or the SIMAP furnace for a better temperature precisio. This allows to perform in situ compression test with controlled temperature (a thermocouple is just underneath the sample) for the study of amorphous metallic composites (see scientific application) with quite fast acquisition of 3s per scan in continuous acquisition mode.
- Furthermore because the NOVITOM machine cannot be used on the HR tomograph and thus limits resolution and speed of acquisition, we developed a device based on NOVITOM concept but that can be mounted on the HR tomograph. The heating can be done with the induction coil or the SIMAP furnace.

Benefit to ID19. These three devices have been designed for fast tomography and are user friendly. They allow performing in situ tomography under mechanical loading at room and high temperature on both HR and MR tomograph : it can be used for a wide range of metallurgical studies and it will certainly be used in the future at ID19.

		
<p>Figure 5 : new room temperature compression/tensile device for fast tomography on the MR tomograph</p>	<p>Figure 6 : NOVITOM machine for high temperature in situ compression/tensile tests for the MR tomograph</p>	<p>Figure 7 : SIMAP machine for high temperature in situ compression/tensile tests for the HR tomograph</p>

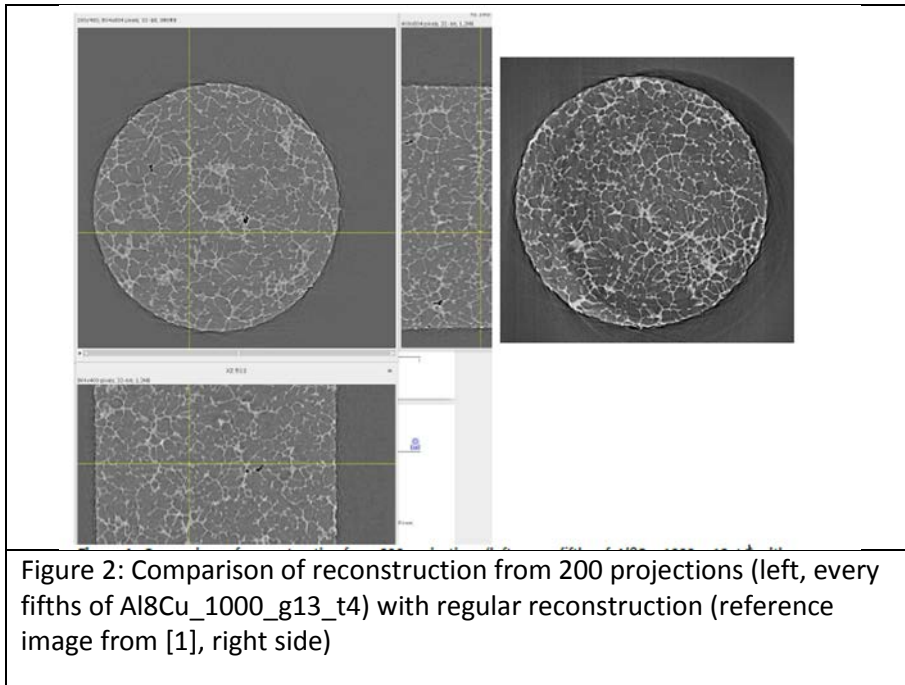
Task 1.3.2 : GPU implementation of new algorithm

A priori knowledge reconstruction in PyHST2 : E. Guillard (SVI), A. Mirone (ESRF) : work has been done concerning the iterative reconstruction with a priori knowledge. The implemented a priori knowledge techniques are based on the total variation penalization and a new recently found convex functional which is based on overlapping patches. Details of the different methods and how they are implemented in the PyHST2 code can be found in the paper of A. Mirone . An interesting point is that they provide methods for estimating, in the absence of ground-truth data, the optimal parameters values for a priori techniques.

Low number projection reconstruction (J. Dittman University of Würzburg) : using database of scans that were acquired at the beginning of the LTP a work was done.

Selected examples from the Tomography examples database LTP ma1876 [1] have been reconstructed down to 200 projections by the total variation minimization approach to Compressed Sensing presented in [2]. As objective quality assessment local thickness analysis based on these reconstructions from few projections are presented. Further, a first result on smearing artifact reducing reconstruction (K. Dremel, LRM / Uni Würzburg) from 250 projections is shown. The respective datasets are Al8Cu_250_g13_t1 (spanning approx. 0.7° per image, 3.9ms exposure) and subsets of Al8Cu_1000_g13_t4 (spanning approx. 0.18° per image, 3.9ms exposure) [1]. Provided results were multi-EDF-type files containing the raw camera images as well as corresponding dark-and reference images. Dark and reference images were reduced by taking the median over the supplied stack. The reference image was (after subtraction of the dark image) scaled to compensate for the slight mismatch in exposure time to the actual radiographs. Subtracting the dark image also from the radiographs, then dividing by the corrected reference image and taking the negative logarithm finally results in the sinograms that are the basis of the following reconstructions. No further preprocessing steps (denoising, etc.) were applied besides clipping empty spaces.

Reconstruction by means of [2] from 125 or 200 projections (every eighth / fifth projection of Al8Cu_1000_g13_t4) took about 100min for the $804^2 \times 400$ volumes as presented here. This time might be reduced (apart from scaling up the hardware) by either precise tuning of the input parameters and/or loosening quality demands. Visually, the compressed sensing reconstructions from few views show more pronounced edges of the thin dendritic structures which appear blurred in the regular reconstruction from the full dataset. It remains to be discussed whether this impacts on the precision of quantitative thickness or volume fraction analyses. While the visual impression as well as the segmentability (by global Otsu threshold) are very good for the 200 projection result (fig. 2 and 3), the reconstruction from 125 projection shows notable visual quality degradation (fig. 4). Regarding the local thickness [3, 4] statistics of the dendrites though, both reconstructions show similar results (with high variance). Additionally, reconstruction from the azimuthally averaged projections Al8Cu_250_g13_t1 was attempted. Figure 5 compares the results of reconstruction analogous to the previous datasets as well as an iterative reconstruction method that reverts the azimuthal integration (K. Dremel, LRM / Uni Würzburg).



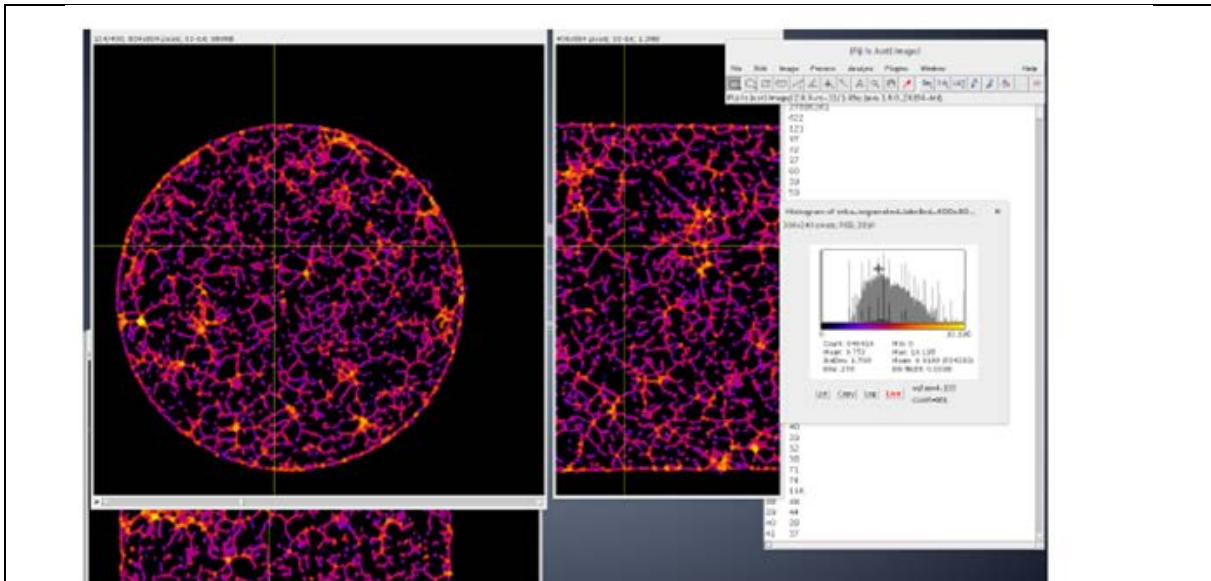


Figure 3: Local thickness analysis of the 200 projections reconstruction shown in fig. 1 (left). The histogram shows the thickness distribution within the visible axial slice. The typical thickness is around 4.2px (= 4.6 μ m).

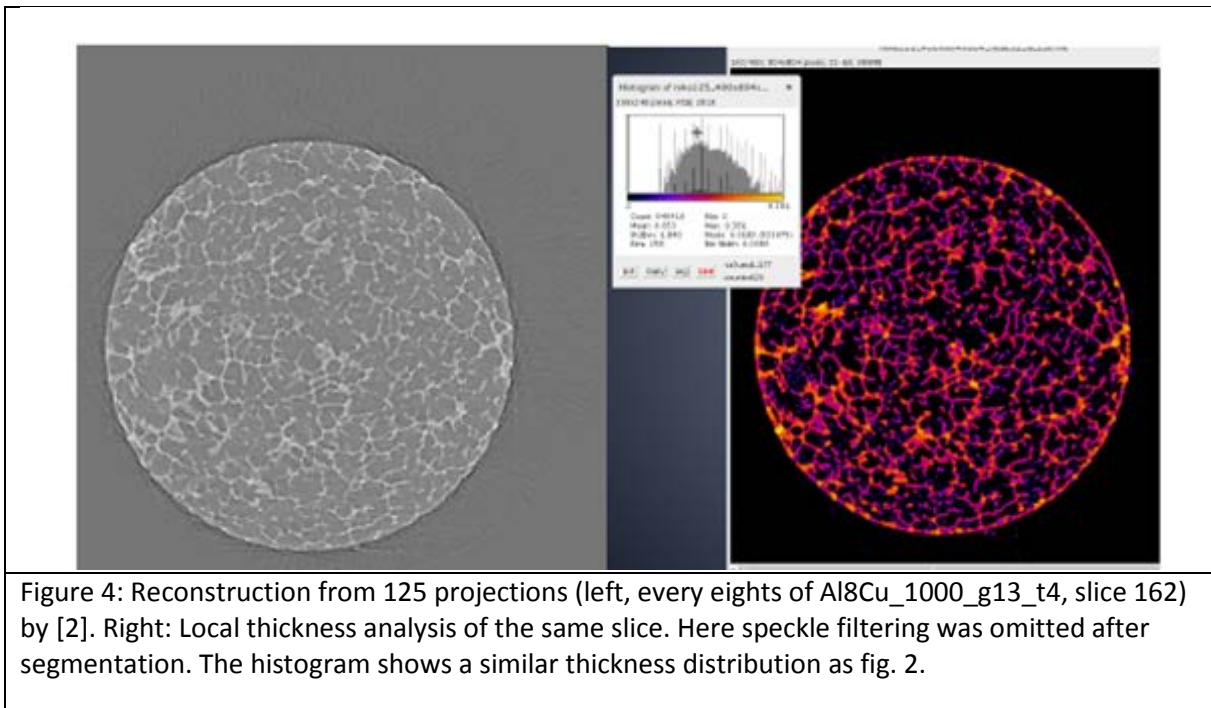


Figure 4: Reconstruction from 125 projections (left, every eights of Al8Cu_1000_g13_t4, slice 162) by [2]. Right: Local thickness analysis of the same slice. Here speckle filtering was omitted after segmentation. The histogram shows a similar thickness distribution as fig. 2.

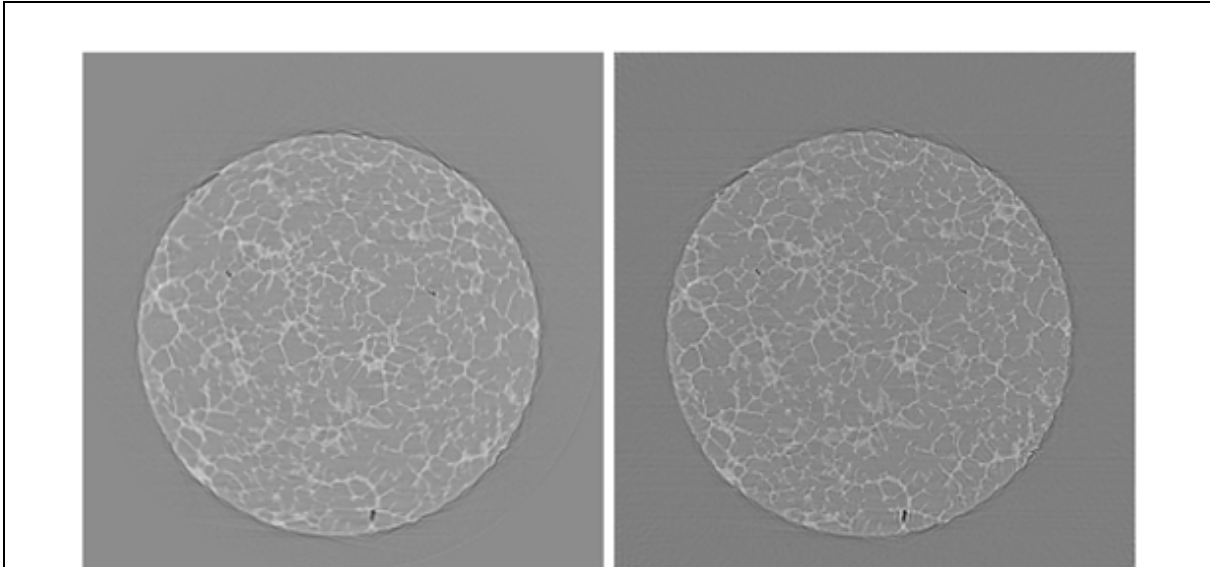


Figure 5: Reconstruction from 250 azimuthally integrated (0.7°) projections (Al8Cu_250_g13_t1). Left: Total variation minimizing reconstruction [2]. Right: smearing artifact reducing reconstruction (K. Dremel, LRM / Uni Würzburg)

[1] Tomography examples database LTP ma1876, <pierre.lhuissier@simap.grenoble-inp.fr>

[2] J. Dittmann, Tomographic reconstruction from few X-ray projections based on compressed sensing, Master Thesis, Universität Würzburg, 2013

[3] Bob Dougherty, Local Thickness ImageJ Plugin, http://www.optinav.com/Local_Thickness.htm

[4] T. Hildebrand, P. Rüesgsegger, A new method for the model-independent assessment of thickness in three-dimensional images, J. of Microscopy 185 (1996)

multi resolution reconstruction : J. Dittman (Univ of Wuerzburg) / M. Ullherr(LRM)

Fast decaying protein foam structures were scanned at two different resolutions (and fields of view) simultaneously at the ESRF ID19 beamline as part of the LTP ma1876 project in November 2014 and analysed in 2015 (table 2). Each dataset consists of 1000 high resolution (HR, $\sim 1.2\mu\text{m}$ / pixel) as well as 1000 medium resolution (MR, $\sim 5.8\mu\text{m}$ / pixel) radiographies acquired within 1s. The respective fields of view (FOVs) are approximately 2.4mm and 1.2cm. Both are region of interest (ROI) scans approximately at the center of a 4cm wide sample column. As required for the dual detector setup, the beam energy was at 60keV which is otherwise disadvantageous for foam imaging. In the following, problems that arose during merging of the data based on the techniques described in [1] are discussed and volume reconstructions of two exemplary merged and phase-retrieved datasets are presented.

<i>Experimental Setup</i>	Micro	Macro
Energy	60keV Pink Beam	60keV Pink Beam
Optics	"9x" Optique Peter	"1.9x" Rodenstock
Camera	PCO dimax	PCO dimax
Scintillator	25 μm LuAg	250 μm LuAg
Effective Pixel Size	1.2 μm	5.8 μm
Exposure Time / Scan Time	1ms / 1s	1ms / 1s
Control & Readout Software	SPEC	PCO Camware
Trigger Mode	Slave	Master

Table 2 : experiments for the multiresolution analysis

Preprocessing. Provided are unsigned 16 bit integer mutli-EDF-type files (HR scan) and single TIF-files (MR scan). No dark and reference (flatfield) images were acquired. While the former is neglected in the processing, the reference image is approximated by the median over all radiographies. As the images are dominated by phase contrast fringes rather than absorption the median is expected to yield a good approximation of the reference image.

Alignment and Merging. In order to merge the MR and HR scans, first the relative positioning as well as the effective pixel size ratio of the detectors need to be known precisely. The latter was determined by several manual distance measurements within preliminary separate MR and HR reconstructions to about 0.4% precision (factor 4.77 ± 0.02). Absolute detector shifts of the individual datasets were as well determined visually by means of reconstructed slices to about 0.2% precision ($\pm 4\text{px}$). The relative horizontal and vertical positioning of the detectors is retrieved from the data by manually guided (visual inspection within reconstructed volumes) image correlation of corresponding radiographies of the HR and MR scans. With known alignment parameters, the radiographies of both scans are finally merged in the fourier domain. Gradual blending in the overlapping frequency domain is used to reduce artifacts.

Phase Retrieval. Both MR and HR scans show significant phase contrast. The free parameter of the Paganin phase retrieval filter (cf. [1, 2]) is estimated by visual inspection in the reconstructed volume for each scan independently to (estimated) 50% precision. The MR radiographies are then prefiltered *before* merging with the HR scan to account for the difference in the determined phase retrieval parameters (cf. [1]). Final phase retrieval filtering is done after the previously described alignment and merging process.

Results and Discussion. Two exemplary datasets were reconstructed from combined HR and MR scans. First dataset contains few large pores (aged foam), i.e. simple structure that can easily be matched. While this dataset doesn't benefit from a high resolution scan due to missing small scale structure (see figure 7), it was used to get first estimates of the relative positions and magnification ratio of the two detectors. Second dataset however shows a typical polydisperse foam with pores down to $\sim 10\mu\text{m}$ diameter and represents a use case of high speed simultaneous multiresolution scans (see figures 9 and 10). This dataset further showed an unexpected sinusoidal relative detector motion synchronous with the rotation stage resulting in a virtual displacement of the rotational axes between MR and HR scan about 0.13mm (cf. figure 8). The cause of this motion remains to be explained. It should particularly be noted that there might also be quality degradations due to additional uncorrelated motions. While, particularly for second dataset, the HR scan indeed yields a resolution gain with respect to the MR scan, the resolution of both scans stays significantly below their respective detector pixel pitches due to the very low SNR in the raw data. While phase retrieval is able to notably improve visual quality due to its low pass property, both scans can be downsampled by a factor 2 to 4 without loss of information.

Conclusion and Outlook. The feasibility of dual resolution reconstructions from simultaneously acquired MR and HR scans is demonstrated including the treatment of mismatching phase propagation distances. The determination of the magnification ratio and relative positions of the two detectors required significant manual intervention for the present datasets and is rather imprecise. It is strongly suggested

to do suitable calibration scans upfront for future experiments. The cause of the observed relative detector motion remains to be investigated.

The actual resolution of both the MR (medium resolution at wide FOV) and HR (high resolution within limited FOV) scan suffered from the bad SNR. The latter is caused by the combination of low absorption (high energy), short exposure time (high speed for dynamic samples) and high resolution (thin scintillator and small pixels). The desired resolution of the HR scan will determine both the necessary exposure time and in consequence the sensible time scale of the dynamics to be observed. While the wide FOV MR scan effectively reduces boundary artifacts within the HR FOV with respect to the long range Paganin phase contrast filter, it remains to be investigated to what extent general CT ROI artifacts within the HR ROI can be eliminated or reduced by the MR scan. The present data didn't visibly benefit in this respect, although this might also be due to the imprecise matchings as well as bad SNR of the scans. Also, the MR scan was a ROI scan as well in this study.

Figure 7: Multiresolution reconstruction (center slice) of first dataset. The reconstruction is limited to 50% (diameter) of the full MR FOV. While the coarse structure doesn't benefit from the HR ROI, the dataset was well suited for first estimates of the geometry parameters and a general proof of concept. In contrast to second dataset, the MR and HR scans didn't show displaced rotational axes, as expected from the experimental setup. Furthermore, the phase retrieval parameter wasn't tuned and phase contrast fringes are still visible.

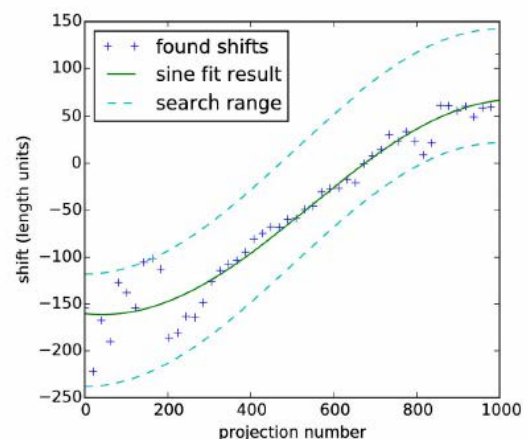
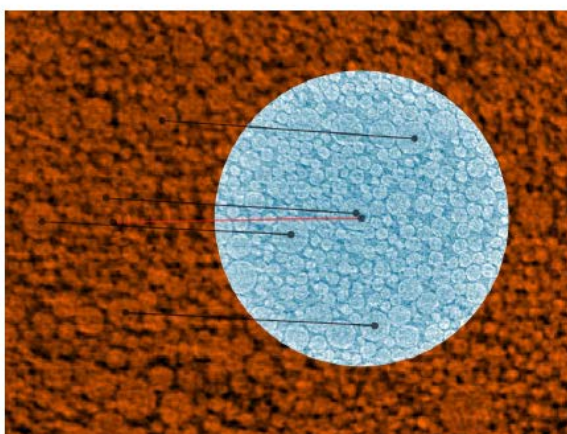
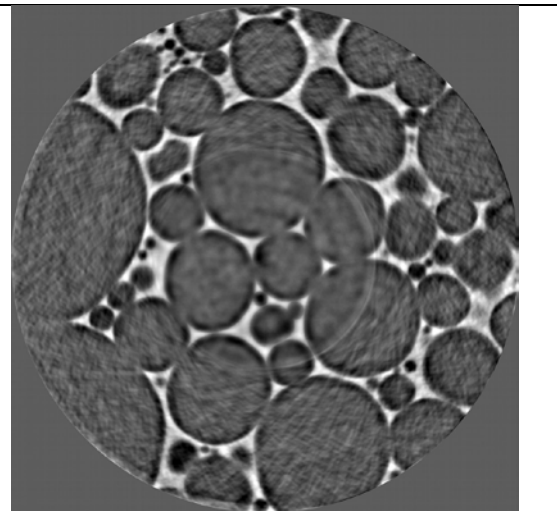


Figure 8: Matching of MR and HR scans (experiment 2). Left: Visual identification of image features between MR (background, orange) and HR (blue inset). Note that that the axes of rotation, visible by the ring artifacts, are not identical. Right: Result of 2D image correlations of MR and HR radiographies. The sinusoidal drift of the relative detector shifts is consistent with the displaced rotational axes, although the fit curve slightly underestimates the observed displacement about 15%. See Results and Discussion for further interpretation.

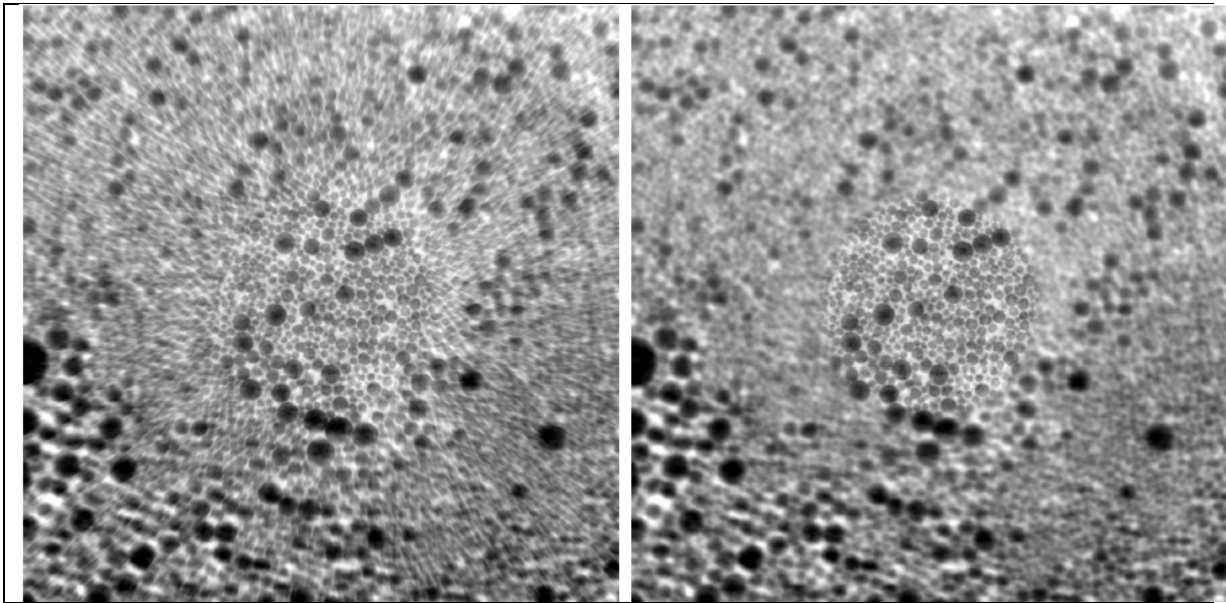


Figure 9: Axial slices of the reconstructed volumes based on merged and phase retrieved HR and (upscaled) MR radiographies (dataset 0046). The reconstruction is limited to 80% (diagonal) of the MR FOV. Left: Reconstruction from merged radiographies. The HR ROI also visibly impacts the MR ROI. The streaking artifacts are limited angle effects of the HR radiographies outside the HR ROI. The slight mismatch of contours of HR and MR information is due to the remaining imprecision of the geometry parameter estimates (relative size and position of MR and HR detector). Right: For comparison, the MR ROI is replaced by a separate MR reconstruction.

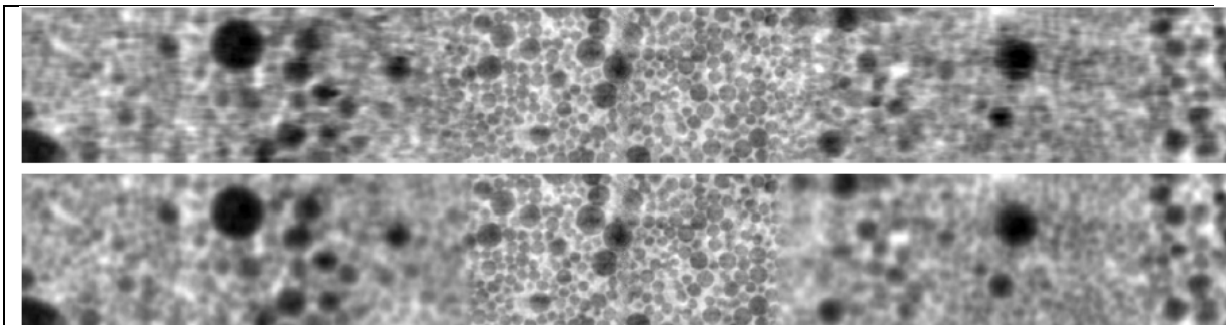


Figure 10: Vertical center slices of the reconstructed volumes based on merged and phase retrieved HR and (upscaled) MR radiographies (dataset 0046). The reconstruction is limited to 80% (width) of the MR FOV. Top: Reconstruction from merged radiographies. The HR ROI also visibly impacts the MR ROI. The artifacts partly result from imprecise geometry parameters (relative size and position of MR and HR detector). Bottom: For comparison, the MR ROI is replaced by a separate MR reconstruction.

Benefit to ID19. This work is of particular interest since a triple mic will be acquired during the LTP as mentioned above and thus multiresolution scans will be certainly used a lot in the future on ID19 and such correction could improve the data providing SNR is better. Furthermore the development of low number projection reconstruction could be of interest for future implementation in PyHST2.

Task 2 : Scientific applications

Task 2.1 : Elaboration

Task 2.1.1 solidification of Al-Si alloys : R. Daudin, P. Lhuissier, L. Salvo, SIMAP)

Two studies have been investigated : the first one is related to the formation of intermetallics in Al-Si-Fe alloys and the second one related to the impact of nanoparticles on the solidification of these alloys.

- Intermetallics in Al-Si-Fe alloys** : depending on the Fe content the phases that appear during the solidification of Al-Si alloys are different and can be estimated using thermocalc simulation as shown in figure 11. We managed thanks to the implementation of the PCO DIMAX on id19 to perform scan in 0.2s, 0.7s and 1.2s with an optic of 1.1 μ m catching the intermetallics nucleation. We were able to show that when iron content is equal or lower than 1.1wt% there is a good agreement in thermocalc prediction and experiments. However when iron content is higher than 1.1wt% we clearly show that thermocalc prediction is wrong since the intermetallics nucleate after the primary phase. Thanks to the ultra fast tomography it was possible to visualise for the first time the simultaneous nucleation of intermetallic and dendrite when the iron content is 1.1wt% as shown in figure 12.

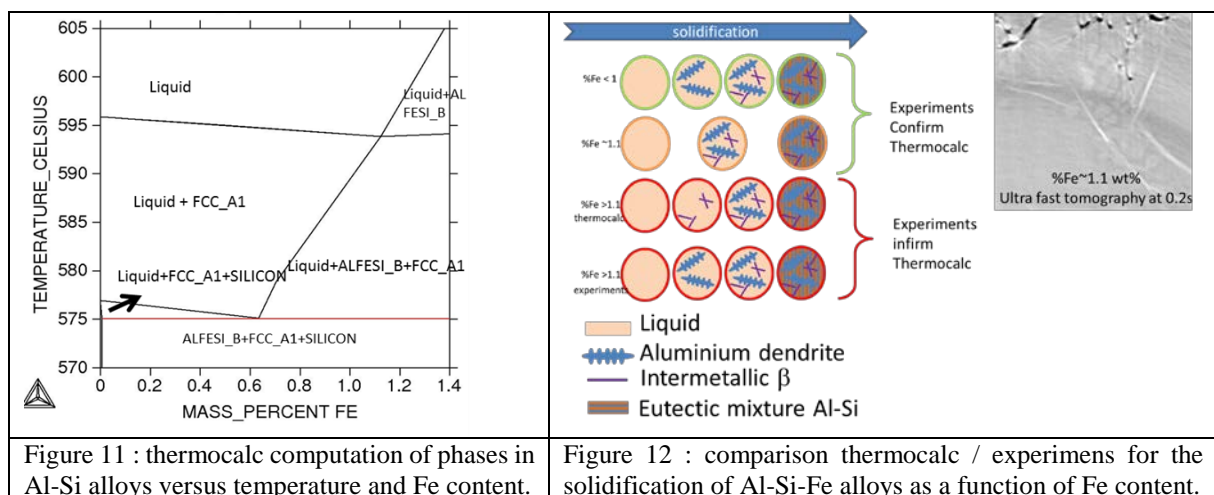


Figure 11 : thermocalc computation of phases in Al-Si alloys versus temperature and Fe content.

Figure 12 : comparison thermocalc / experiments for the solidification of Al-Si-Fe alloys as a function of Fe content.

- Nano composites** : The material was provided by BCAST institute from Brunel University. The incorporation of 1wt% (0.54 vol%) Y_2O_3 particles (~ 500 nm) in the molten Al-6082 matrix was performed under mechanical stirring (at about 350 rpm). Ultrasonic melt treatment was applied for 5 minutes at a frequency of 17.5 kHz. The *in situ* tomography experiment was carried out at the ID19 beamline of ESRF. The sample was glued at the top of an alumina rod fixed on a rotating stage. A resistive furnace mounted on a translation stage above the rod can be moved down allowing the samples to be remelted. It is equipped with two windows made of glassy carbon to allow X-rays passing through. A dedicated optic system with a x20 optic and LuAG scintillator was placed in front of the camera. The latter is a PCO Dimax allowing fast acquisition imaging. The tomography scans were performed with a pink beam of 17.6 keV by recording 1440 images over 180° with an exposure time of 3.10^{-3} s (i.e. a total scan time of 4.3 s). The field of view was 1920x1440 pixels and the pixel size 0.55 μ m. Hence, the total volume area recorded in each scan is 1.6x1.6x0.8 mm³. Each 3D image was recorded every 1.5 minute which is the necessary time to

save the data and 38 consecutive 3D images were recorded in time during the overall melting-solidification procedure (approximately 1 hour). The heating and cooling rate were set to $5 \text{ K}\cdot\text{min}^{-1}$ and $3 \text{ K}\cdot\text{min}^{-1}$, respectively. The remelting and solidification behaviour of a 6082+1wt% Y_2O_3 composite was investigated by *in situ* synchrotron microtomography.

The main results of this study were published in *Materials and Design* and *Acta Materialia*:

- The Y_2O_3 particles can be revealed by remelting the sample and dissolving the eutectic phase. The majority was located at the grain boundaries suggesting that most of them were pushed by the solidification front during casting. Few yttria particles were nevertheless found in the matrix, i.e. engulfed in the primary solid phase (see figure 11)
- Above the liquidus temperature, stable branched networks of Y_2O_3 particles associated with pores were observed in the molten matrix (see figure 11).
- Upon solidification at low cooling rates, these Y_2O_3 aggregates were pushed by the solidification front and squeezed between dendrites to eventually end up in the narrow eutectic region (figure 12).
- Nanoparticles when they are well dispersed using the *in situ* Ultrasonic device before the solidification experiments influences largely the shape of dendrites (figure 13) and this is attributed to the interaction of the nano particles with the solidification front. Note that this is the first experiments showing this phenomenon in metallic alloys and in 3D.

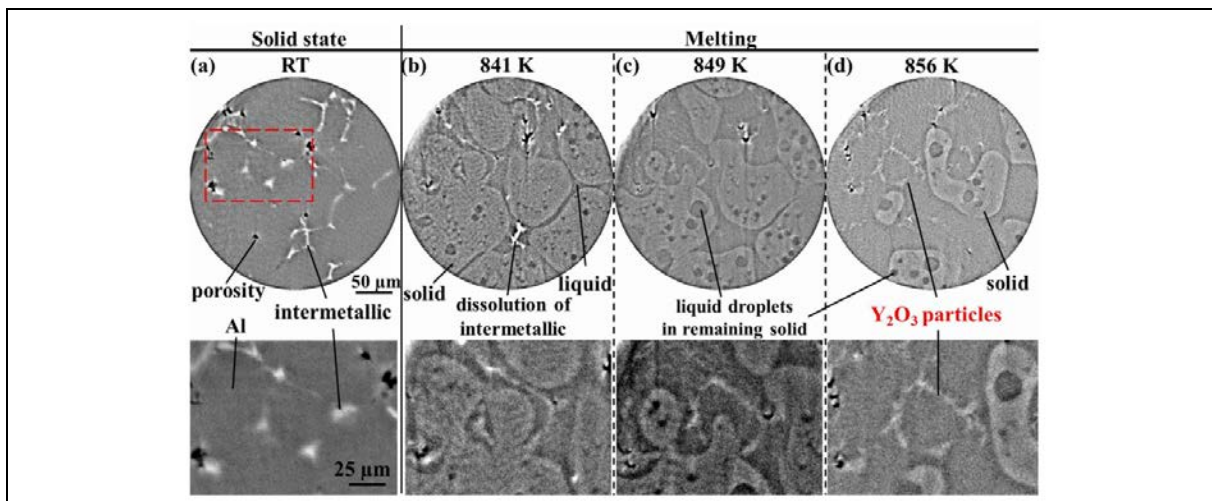


Figure 12; Sequence of 2D images extracted from the volume of the specimen showing the evolution of the microstructure during remelting: (a) room temperature where Y_2O_3 particles cannot be distinguished; (b) 841 K; (c) 849 K; (d) 856 K. The bottom part is a zoom of the region highlighted by the dashed box.

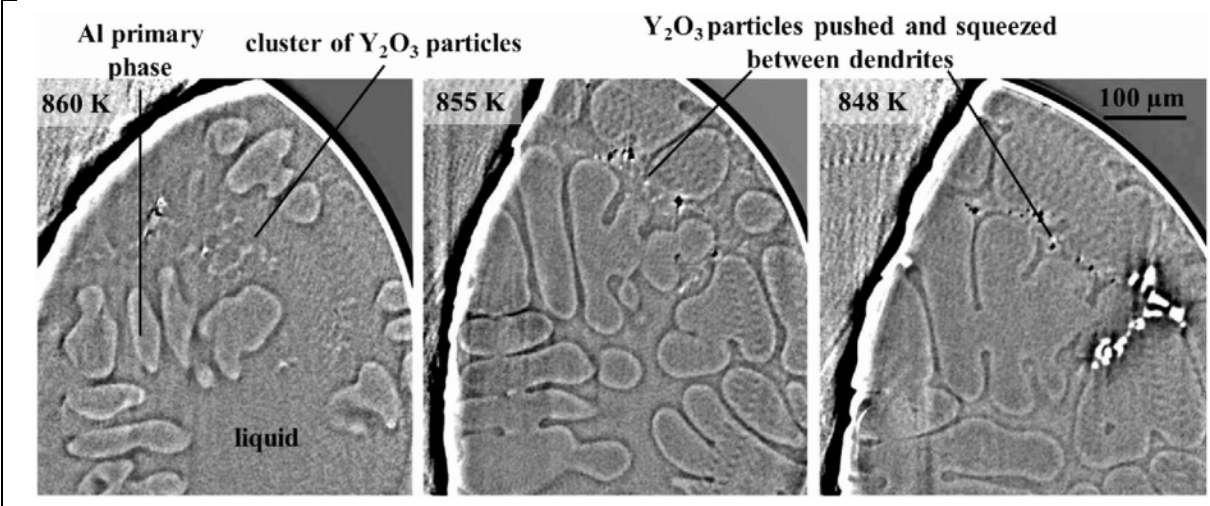


Figure 13 : Sequence of 2D images extracted from the volume of the specimen showing the evolution of the microstructure during cooling from the fully liquid state at 910 K. The growth of Al dendrites can be observed as well as their interaction with clusters of Y_2O_3 particles.

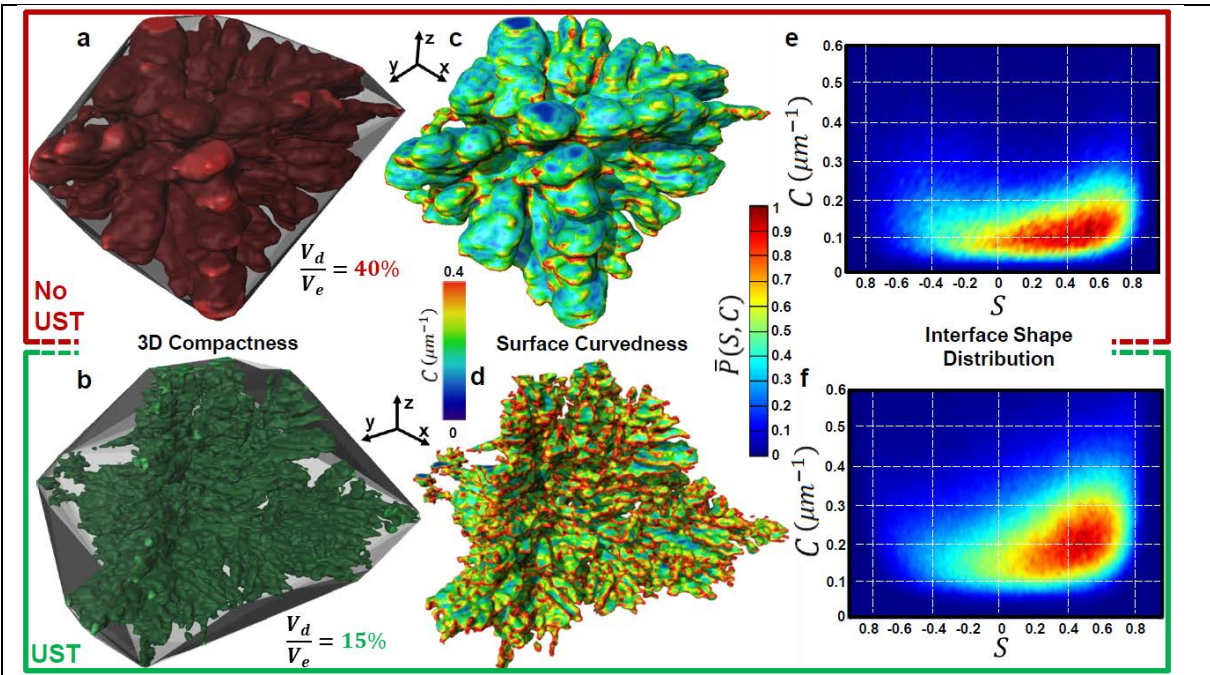


Figure 13 : influence of dispersion of particles on the shape of dendrites : dendrites after 4s of solidification are shown along with the curvature analysis.

Task 2.1.2: foams :

Aqueous foams : J. Dittman (Univ Wuerzburg)

Aqueous protein foam samples were imaged with high-speed μ CT at ID19 by the LRM Group in collaboration with the Fraunhofer EZRT (Fürth, Germany) and the Technical University of Munich. A custom data analysis technique enabling large scale individual pore tracking in the presence of drainage was developed and tested to facilitate systematic studies on foam dynamics. A prototype of an in-situ foaming device (capable of foaming while rotating) was developed as well and tested in the context of simultaneous multi-resolution acquisition at the ID19.

A foaming device was designed together with W. Wiest and D. Althoff (LRM) based on the following key components:

- A fritted glass filter funnel with 10-40 μ m nominal porosity (P3-P4) and 20-50mm diameter as sparging device. Standard article at chemistry supply stores. See e.g. [1]
- A fitting plastic cylinder as X-ray transparent foaming column.
- A rotary union with little torque for gas transfer Available from DSTI [2]
- An electrical valve that allows remote control of gas flow. Available e.g. from Festo [3]

The particular chosen rotary union by DSTI [4] has a pressure-dependent sealing. At low gas pressures, it is not fully leak-proof but remains easily rotatable with low torque as required by the high-precision rotary stages at ID19. The prototype further contains an aluminum vessel that both serves as support for the foaming column and as reservoir for leaking liquids. The following graphs in Figure 14 shall give an impression of typical results:

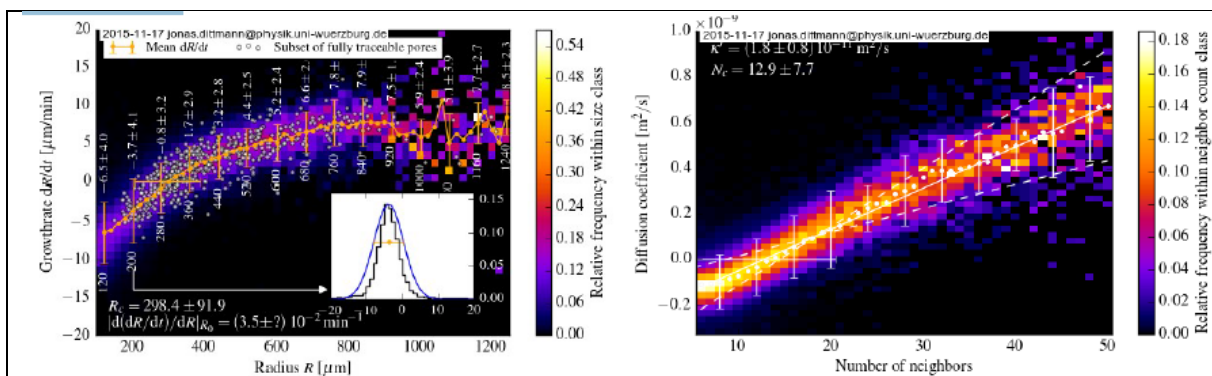


Figure 14: Left: pore radius growth rates derived from traced pores are graphed as a 2D histogram together with mean values, standard deviations zero crossing and slope at zero crossing. Right: The same data is represented according to the Glazier-model [2] with respect to the neighbor count, displaying zero crossing, mean slope (diffusion coefficient) and standard deviations. The presented data was gathered from a total of 5 μ CT snapshots containing between 40 000 and 60 000 pores. Acquisition time was 1s per scan.

Benefit to ID19. The prototype in-situ foaming device in combination with the presented data analysis techniques lay the foundation for a standardized foam dynamics characterization protocol. The developed technique for pore tracking is further applicable to other 3D feature point tracking

problems that arise in dynamic tomography when suitable segmentation and labelling methods for the given problem exist.

References.

[1] https://en.wikipedia.org/wiki/Fritted_glass

[2] <http://www.dsti.com/products/rotary-unions/It/>

[3] <http://www.festo.com>

Metal foams (F.G Garcia Moreno HZB)

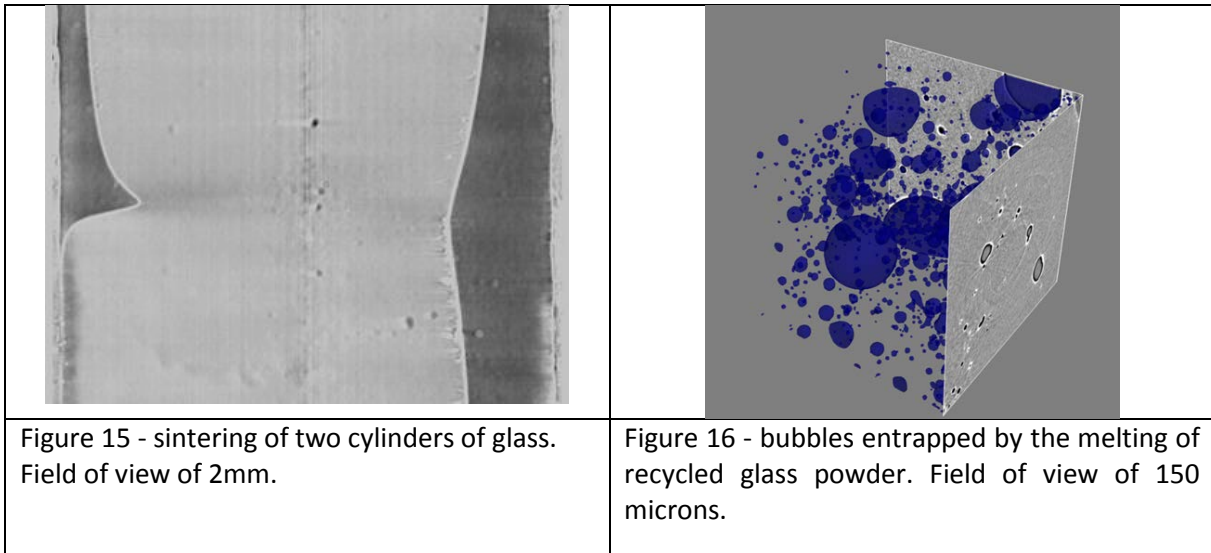
Aluminium alloy foams are created by injecting gas containing different levels of oxygen (from <<1 ppm to 21%) into melts stabilised with SiC particles. Individual liquid aluminium alloy films meant to represent the films in a foam are produced of the same materials. In both cases the oxygen concentration of the atmosphere is controlled too. Synchrotron X-ray radiography on Al liquid films is applied to track the movements of the particles in liquid films and to observe how they flow, pile up and form clusters. Experiments on Al foams show that only when the injected gas and atmosphere contains oxygen foams can be expanded continuously. In contrast, if foaming is carried out by injecting argon into the melt and the Ar atmosphere is free of oxygen no stable foams can be created, even if the melt contains 20 vol.% SiC. It is concluded that not only particles are required to allow foaming, but also the formation of an oxide skin is necessary and the combination of both are the basis of foam stabilisation.

Task 2.1.3 : glass formation (E. Gouillart SVI)

Nucleation and growth of bubbles in molten silicate glass (PhD Damien Boloré)

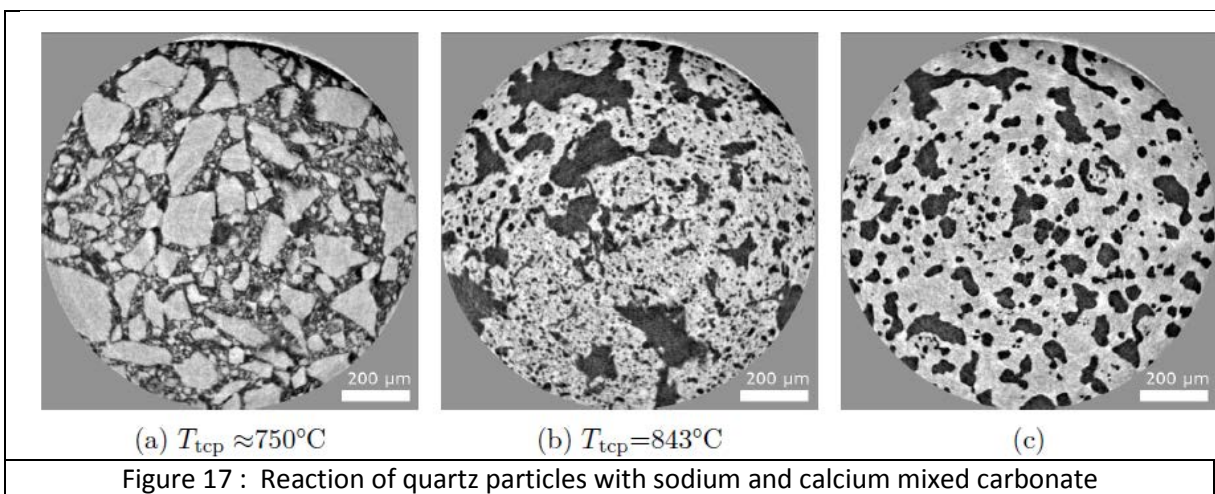
Using recycled glass in bottle-glass furnaces lowers the energy cost of glass melting compared to crystalline raw materials, yet high temperatures (1500°C) must be used to get rid of entrapped bubbles. Several types of bubbles form in the glass melt: bubbles coming from entrapped gas pockets and bubbles originating from chemical reactions. The monitoring of the nucleation and growth of bubbles in molten glass is difficult as high temperatures, and in-situ microtomography is a tool of choice to observe such phenomena.

It has been reported that sulfur is responsible for the creation and the growth of bubbles in glass melts. In order to investigate the mechanisms between the different oxidation states of sulfur in glass, we put in contact glasses with different oxidation states of sulfur at high temperatures. In situ tomography then allows us to observe the interface and the nucleation of bubbles at microscopic scales (Figure 15). In other experiments, we can use in situ tomography to reconstruct a granular material composed of glass grains during its melting, and observe the closing of the pore network (Figure 16).



Reactivity of glass batch materials at high temperature (PhD William Woelffel)

We investigate the kinetics and geometry of chemical reactions between powders of glass raw materials (quartz sand, sodium and calcium carbonate). In particular, we observe the formation of silicates in the course of decarbonation reaction when carbonates are in contact with silica. Since the kinetics of such reactions strongly depend on the surrounding atmosphere, we use the controlled-atmosphere induction furnace co-developed at ESRF. In February 2015, we did a first campaign using this furnace with a continuous flow of CO₂ and continuous rotation of the furnace and sample. Figure 17 shows cuts of the same sample at different temperatures, for a mixture of quartz grains and mixed sodium and calcium carbonate. We observe that the reaction only starts at the eutectic temperature of the mixed carbonate (image b), and that a solid precipitates immediately. Other similar experiments shed light on the existence of several reaction paths that depend on composition and geometry. A journal paper is currently being written on these results and should be submitted in the next coming months.



Phase-Task 2.2 : Phase transformation

Task 2.2.1 : Crystalline ordering in micro-foams(A. Meagher, F.G. Moreno, HZB)

Nanoindentation is a material characterisation technique by which the hardness of a substance is determined from the force-load curve produced when a tip, of particular shape, is pushed into a sample of said material. Such characterisation has been successfully studied theoretically using the Bragg bubble raft model of crystalline interactions. However the limitations of a two dimensional system frustrates the exploration of many phenomena unique to three-dimensional systems. The development of high-energy X-ray facilities, along with advanced imaging and three-dimensional printing, has allowed us to finally expand these experiments into three dimensions. Firstly, the expansion and proliferation of rapid-prototyping machines has allowed us to fabricate indentation tips precisely scaled to the bubbles we are employing in our experiments. The advances in X-ray imaging has provided us the sensitivity and time-widows required to conduct this delicate work. Figure 9 shows a radioscopic image of one of our indentation experiments. Bubbles of approximately 800 microns in diameter are seen to order at the top of the vessel, while the indentation screw is seen at the bottom of the image. A top the indentation screw an indenter tip with a Vickies style geometry is place. However, due to the relative absorption profiles of the polymer used in construction and the aqueous solution in which the bubbles are placed, this indentation tip cannot be resolved in the radiographies. So far our experiments have met with mixed success. Our initial experiments were met with several technical problems which led to uncertainties in the validity of our experiment. Our last synchrotron campaign had resolved these difficulties however. The foams were produced correctly, the indenter tip was positioned successfully beneath the bubble pile and the resulting indention process was conducted smoothly and in a controlled manner.

Experimental conditions : pink beam, PCO Dimax with FoV 20 x 10 mm, pixelsize 10 μm .

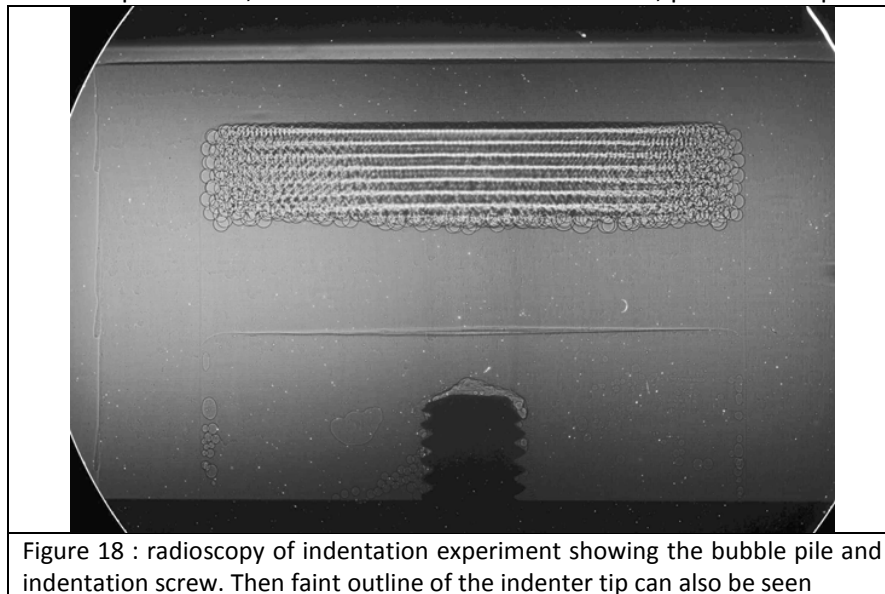


Figure 18 : radioscopy of indentation experiment showing the bubble pile and indentation screw. Then faint outline of the indenter tip can also be seen

Later, while reconstructing the samples an unusual imaging defect was discovered. While the exterior of the sample could be successfully reconstructed, the interior of the sample was found to suffer from an apparent blurring effect (Figure 19). More unusual still, these defects were only present on certain image slices (Figure 20). Such noise produced significant errors when segmentation of the images was attempted, leading to results which could not be trusted for determining statistical properties about our foams. The result is that, while our experiment proceeded without fault, the current results can

only yield qualitative results regarding the structure of the foam and how this changes during the deformation of the sample.

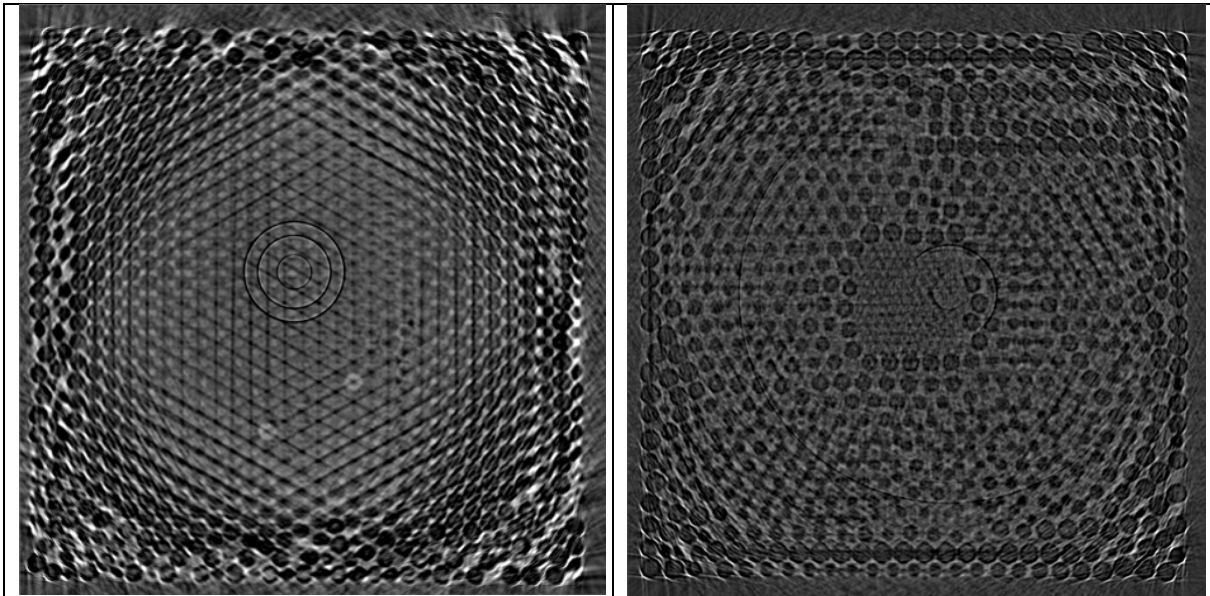


Figure 19 : Foam reconstruction showing the imaging artefact leading to errors during the segmentation process. Near the boundaries of the foam, a clear distinction is seen between the liquid (white) and air (black) phases of the foam. Near the centre of the foam this clear distinction is no longer present.

Figure 20 Another reconstructed slice of the same foam. The foam is seen to be broken into crystalline regions, while the square section in the centre of the image shows a cross section of the indenter tip itself. The image noise problem in Fig.2 is no longer seen. The edge-length of the cell is 20 μm .

We hope to be able to repeat this experiment in the future. With proper imaging parameters in place, and a smooth experimental procedure, we expect to perform our experiments successfully. The resulting experimental data will represent a significant advancement within the area of foam physics, and its expansion into the domain of simulation media for other systems.


Task 2.2.2 : Intumescent coatings

Characterization and dynamics : C. Simpson, X. Zhong, P. Withers (Manchester University) :

After the successful preliminary tests presented in the previous report new experiments were performed during a classical proposal.

The session was performed on 3rd Nov 2015 (MA2774) with the aim to have a more detailed and systematic study (Phil Withers, Yong Wang, Alexander Rack, Christopher Simpson, Serafina Garcea and Xiang li Zhong). Samples were prepared using the same procedure described for the first experimental session. However, in this session the specimen was not heated by the heating stage, but the sample was directly placed in a furnace. The temperature range used was 200-400 $^{\circ}\text{C}$, and the heating rates used 5 $^{\circ}\text{C}/\text{min}$ and 50 $^{\circ}\text{C}/\text{min}$. The scans were performed for each temperature increment (every 5 $^{\circ}\text{C}$ and 50 $^{\circ}\text{C}$ respectively), starting from 200 $^{\circ}\text{C}$ until 400 $^{\circ}\text{C}$. The voxel resolution chosen was 2.75 μm , allowing a maximum field of view of ~ 5.5 mm. The energy level used was 19 keV. The number of scans per second is connected with the capability of the camera, which in turn is directly associated with: (i) the region of interest (ROI), (ii) the number of projections, and (iii) the exposure time. Capturing

dynamic effects, such as the bubble nucleation and growth, requires a sampling frequency higher than the physical growth of the bubbles. Various settings, combining the aforementioned parameters, were considered to define an adequate scan configuration, able to capture the dynamic of the process. In correspondence of the maximum temperature, a static scan was also performed, maintained the same number of projections (500), but increasing the exposure time (2.5 ms) and considering the full ROI available (2016x2016). A summary of the scans performed is provided in the Figure 22.

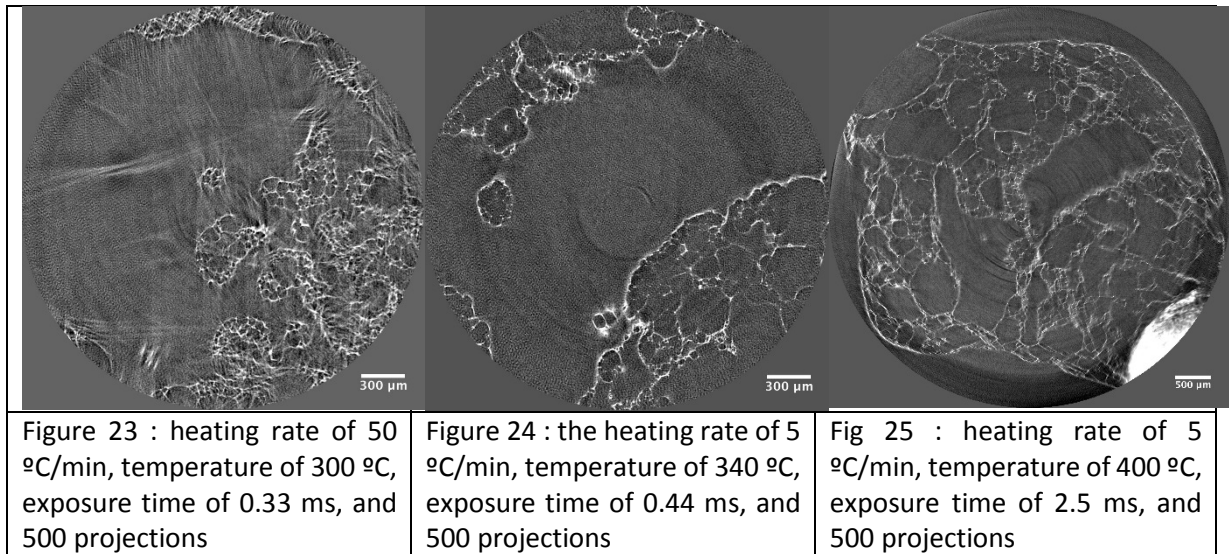
	Heating rate (°C/min)	Exposure time (ms)	Number of projection	Region of interest
	50	0.78	500	2016x2016x2016
	50	0.44	500	1008x1008x2016
	50	0.33	500	1008x1008x1500
	50	0.25	500	816x816x1048
	5	0.78	500	2016x2016x2016
	5	0.44	500	1008x1008x2016
Static scan	2.5	500	2016x2016x2016	
Figure 21 : heating device for the intrumescent foams mounted on ID19	Figure 22 : Summary of the parameters used for the various cases considered during the second experimental session.			

The growth of the bubbles after their nucleation was very fast, resulting in motion artefacts, particularly for the heating rate of 50 °C/min, as shown in Figure 23. The image quality obtained (noise associated with the limited number of projections and the low exposure time) does not allow segmenting the boundaries between neighbouring bubbles using automatic techniques even when the low heating rate is considered (5 °C/min), see Figure 24. Nevertheless edges are visible and distinguishable by human eyes, the contrast between edges and the background is poor to allow the implementation of automatic segmentation. The noise is consistent lower in the case of a static scan obtained for a temperature (400 °C) that does not correspond to drastic changes of the foam structure, connected therefore with the possibility to increase the exposure time, as visible in Figure 25.

The enhancement of the contrast between the bubble membranes and the background is fundamental to implement a semi-automatic technique for the segmentation of the bubbles. This quantification can provide important insights into the physical process, such as the shape and number of bubbles at the nucleation point, how the merge each other with the growth, bubble burst, estimation of velocity of growth and pressure. These physical observations of the dynamic foaming process on intumescent coating during expansion and the relation with the internal structure can be used to inform models to predict the coating behaviour.

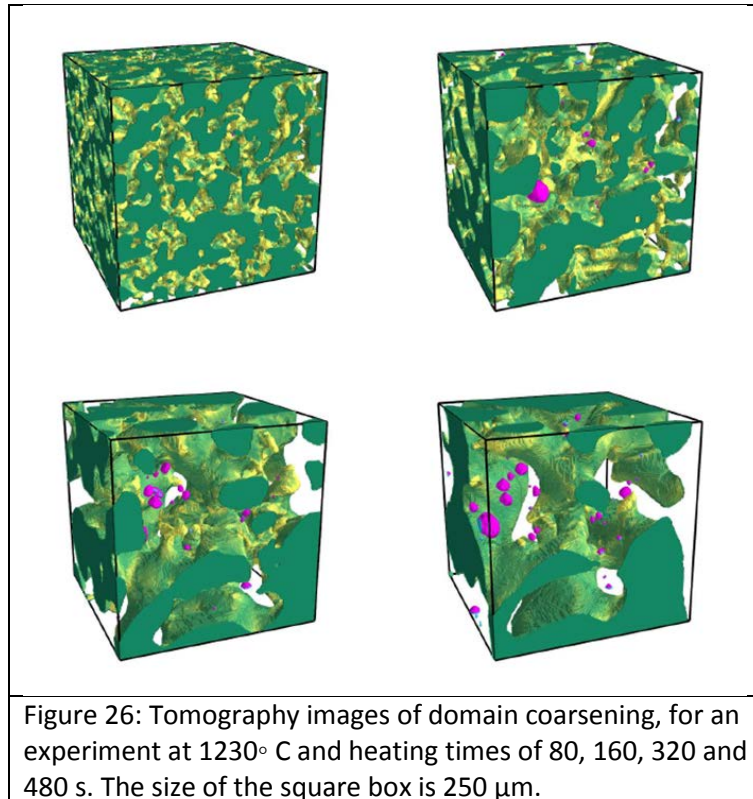
The dynamic scans performed represented the limit achievable using the current technology in terms of duration of a single scan. Therefore, the aim is to obtain the segmentation of the bubbles following

an approach that uses various sub-methods (improving the edge contrast and considering physical laws of bubble growth that can guide the segmentation process). These experiments represent the first use of ultrafast computed tomography to monitor the nucleation and growth of an intumescent coating. Results obtained are promising to assess qualitatively and quantitatively the physical process connected with the internal structure of the foam. In conclusion, this project has enabled the possibility of detailed real time observation and 3D quantification as well as modelling of the dynamic foaming process including coating expansion and internal structure evolution as a function of heating rate. This information on dynamic foaming process of intumescent coating during expansion and internal structure evolution can be used to predict the coating behaviour.



Task 2.2.3 : Phase separation glass

Isothermal and cooling experiments (E. Guillardt SVI) : In June 2014, we performed new experiments on phase separated barium borosilicate glasses (with a larger volume fraction of the phase with the lowest viscosity, compared to earlier experiments). These experiments, together with earlier experiments (MA1281, SC3724), were used to demonstrate the hydrodynamic nature of coarsening in glass melts at high temperature, and in particular the very good agreement between the coarsening rate and the surface tension over viscosity ratio. These results are gathered in a publication that will be submitted in the next few weeks. Figure 16 presents the 3D rendering of the phase evolution during isothermal experiments at 1230°C



Task 2.3 : Materials under loading

Task 2.3.1 : Damage at low temperature

Ductile metals and composites (E. Maire, MATEIS) : Damage characterization in aluminum matrix composites reinforced with amorphous metal inclusions

Composites : The PhD of Antoine Ferré was dedicated to the fabrication of aluminium composites reinforced with spherical Metallic Glass spheres. The samples prepared were then subsequently tested by in situ tensile test to analyse the co-deformation of crystalline aluminium and MG reinforcement. The aim of the PhD was also to understand damage accumulation in these materials. All the tensile tests of the PhD were performed in the frame of the present LTP. Some of the materials produced were rather fragile so it was necessary to use high frequency acquisition during continuous tensile test to fully understand the fracture process. The experimental part of the PhD was published in Materials Science and Technology. Another paper on the modelling part of the PhD is currently in preparation.

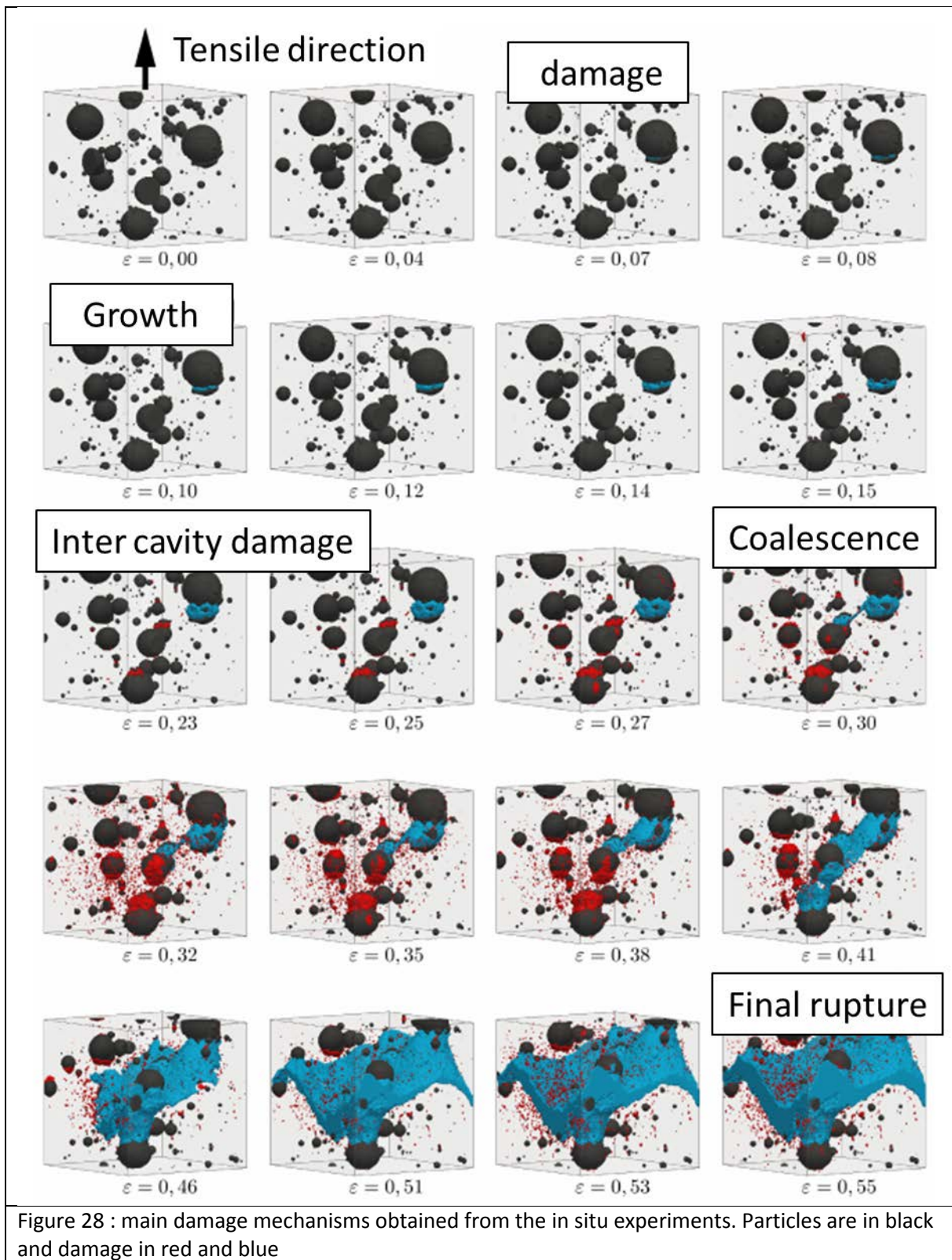


Figure 27 : 3D view of the samples prepared that were submitted to in situ tensile experiments.

The main results obtained from the In situ experiments are :

- There is no real influence of the matrix strength in the damage initiation
- The more the volume fraction of particles the more the less particle rupture are observed
- Particle rupture is mostly governed by their shape and internal defects
- Small particles allow to reduce particle rupture

Figure 28 presents the main mechanism observed during in situ tensile experiments.



Ductile metals : Ductile failure of three 6xxx aluminium alloys has been characterized and modelled for about thirty hardening conditions each. These alloys involve relatively similar composition and volume fraction of second phase particles. The tensile mechanical properties show the expected decrease of

fracture strain with increasing strength but also major differences among the different alloys with a factor ten in terms of reduction of area at fracture between best and worst case. The origin of these differences is unraveled by detailed characterization of the void nucleation, growth and coalescence process involving in situ 3D microtomography performed in the frame of the present LTP. A cellular automaton model, involving a high number of particles with distributions of position, sizes and void nucleation stress has developed to predict the fracture strain. Excellent predictions are obtained based on the same unique nucleation stress distribution versus particle size for the three alloys. The key element setting the fracture strain is the effect of particle size distribution and spatial distribution on the void nucleation and coalescence processes. The dependence of ductility on strength is properly captured as well. Most of the parameters needed to validate the model (particle size distribution, particle spatial distribution), were measured using X ray tomography as shown in figure 29. The results were presented in several papers.

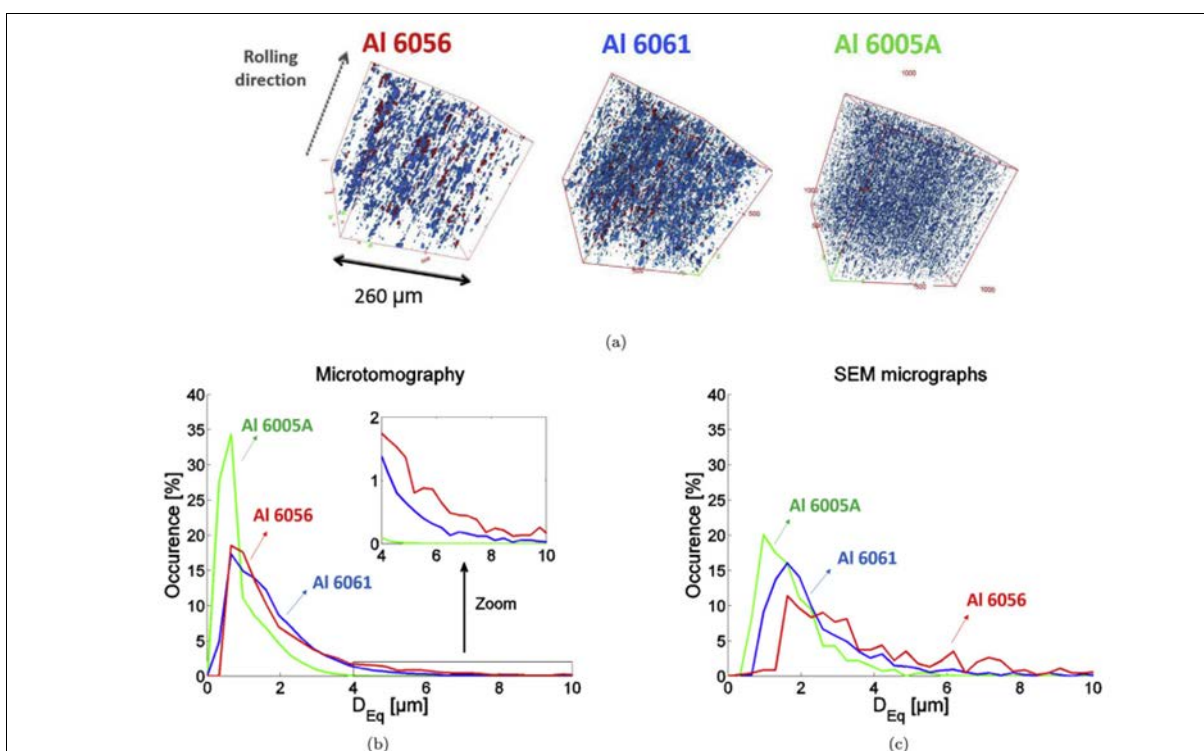


Figure 29 : Characterization of intermetallic particles sizes and initial porosity by X-ray microtomography. (a) 3D microtomography perspective of particles (blue) and pores (red) distribution in all three alloys. Distribution of equivalent diameter for the intermetallic particles; (b) based on the 3D X-ray microtomography images (c) based on the SEM micrographs. (For comparison with CT results).

Task 2.3.3 : Amorphous metal composites at high temperature

Thanks to the new device presented above it was possible to perform compression test experiments of various bulk metallic amorphous composites. The list of experiments are presented below. Acquisition were performed with PCO DIMAX camera at 68 KeV with the 2.75μm optic with scan time of 3s (1000 projection with 1008 x 1008 field of view).

Scan name	sample	Sample comment	Ram speed [$\mu\text{m/s}$]	Strain rate [s^{-1}]	Temp. [$^{\circ}\text{C}$]
cud_50Zr_II_400C	Cuivre – verre métallique	50% VM	0.3	$5 \cdot 10^{-4}$	400
cud_15Zr_I_400C	Cuivre – verre métallique	15% VM	0.35	$5 \cdot 10^{-4}$	400
cud_30Zr_400C	Cuivre – verre métallique	30% VM	0.3	$5 \cdot 10^{-4}$	400
cud_50Zr_I_400C	Cuivre – verre métallique	50% VM	0.175	$2.5 \cdot 10^{-4}$	400
cud_15Zr_II_400C	Cuivre – verre métallique	15% VM	0.0875 0.35 (scan #82)	$1.25 \cdot 10^{-4}$ $5 \cdot 10^{-4}$	400

Figure 30 present in situ compression tests of a composite with Cu and BMG particles.

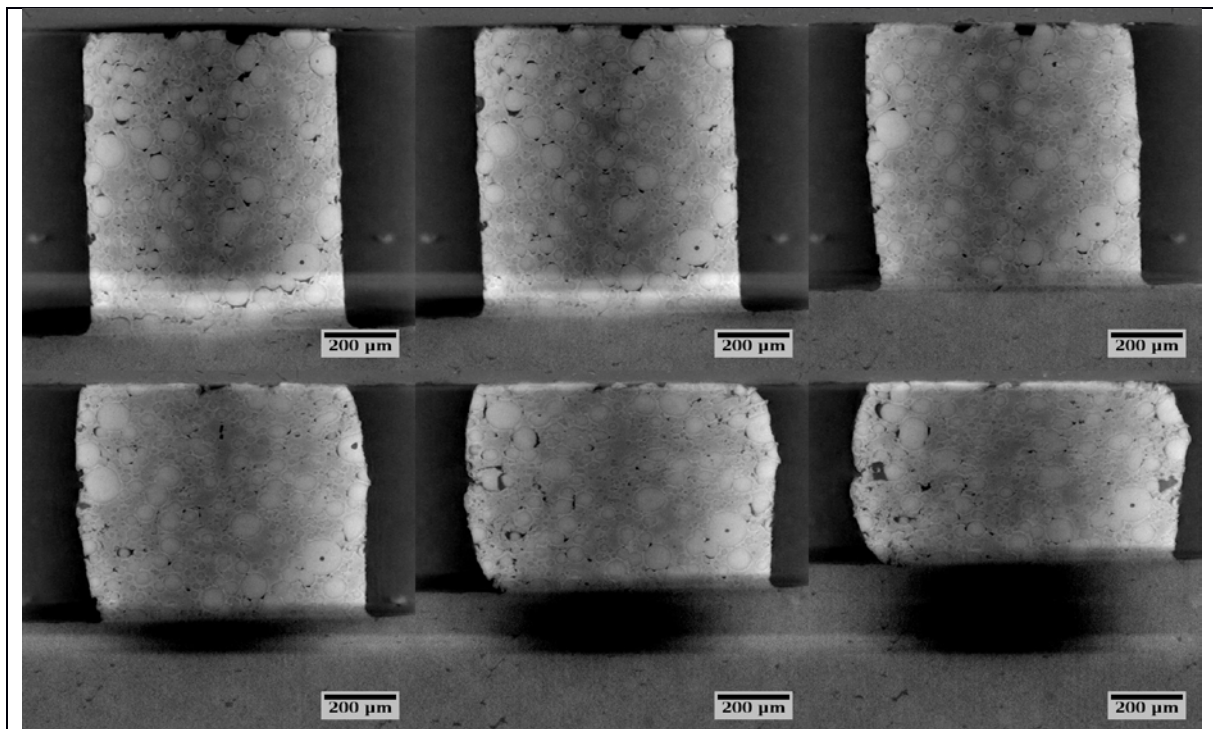
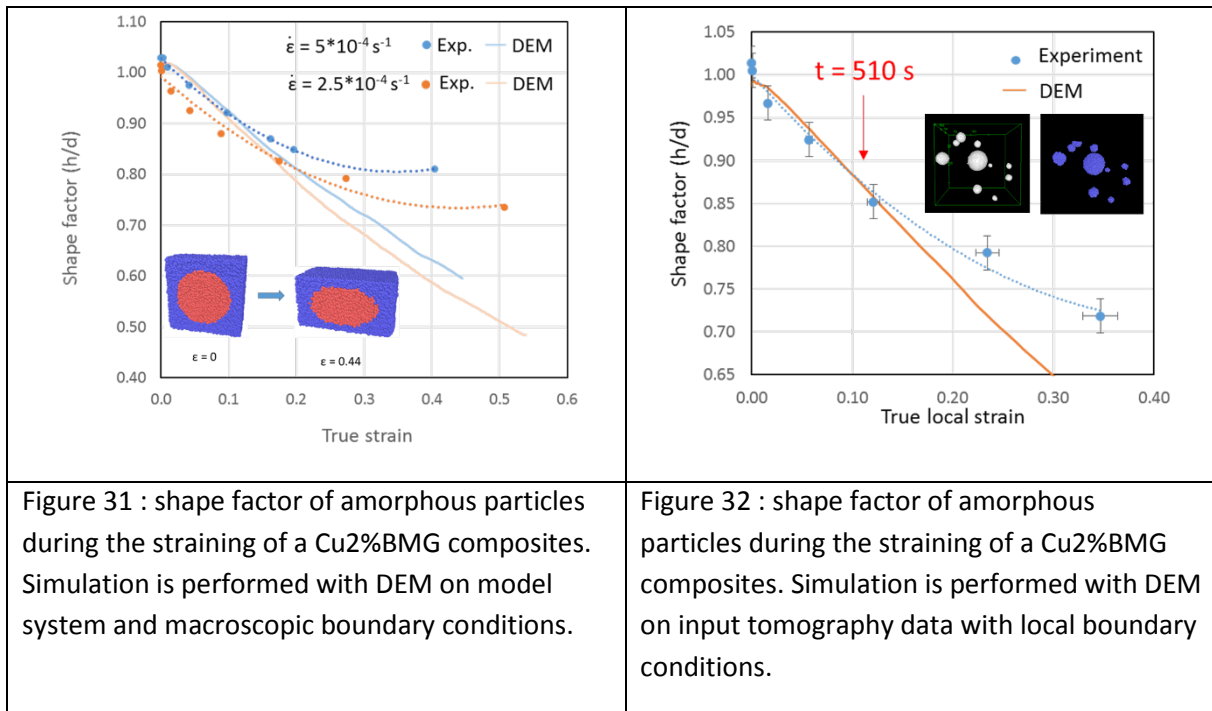


Figure 30: 2D cross sections of a composite sample during a compression test with a strain rate of $5 \cdot 10^{-4} \text{s}^{-1}$ at 400°C imaged in situ by computed tomography.

Full 3D analysis of the experiments allow to define range of strain rates where the two phases of the composites are co-deforming. It was possible to follow in situ the aspect ratio of the amorphous particles and compare it to Discrete Element Method. Figure 31 and 32 present this analysis either applying macroscopic boundary conditions on a model simulation or applying local boundary conditions (extracted from 3D tomography data) and applied to the real in situ data. It is worth noticing that DEM modelling works well except for large strains and this is due to the crystallization of the amorphous particles changing thus their constitutive behavior from soft to hard inclusion.



Task 3 : Dissemination

Task 3.1 : User friendly development

Data acquisition (W. Augustin, R. Daudin, SIMAP/ESRF) : Refurbishment: 'fasttomo' (octave-based reconstruction front-end)

The reconstructions of the data are now handled by the *fasttomo_awerner* macro which is now used currently on ID19 and ID16B (renamed fasttomo3). Details on this function and its associated setup function (*fastsetup_awerner*) can be found on the ID19 wiki¹. Improvements were made on its possibility to reconstruct easily the scans acquired in different conditions (different detectors, different acquisition modes) as well as to tune the reconstruction parameters in a simple way. Apart from the 'live slice' procedure, it is now very convenient to quickly visualize what happens inside the sample. For example:

```
> fasttomo_awerner ('series', [15 1 25], 'fixedslice', 222, 'paganin',1,
'deltabeta',50,'stack','test_scans_15_to_25','ringcorrection','YES','ref_cas
e',0)
```

applied to multiple or continuous acquisition will reconstruct the slice 222 for each scan between scan 15 to scan 25, with a paganin correction ($\delta/\beta = 50$), with ring correction of PyHST and with a computed flat field. All reconstructed slices are put on the fly in an ImageJ stack named 'test_scans_15_to_25'.

A very promising feature of this macro concerns the reconstruction versatility of continuous acquisition. Indeed in this mode, as scans are recorded continuously, there is no gap between groups of projections forming a scan over a range of 180° (or 360°). Consequently, it is possible to choose the

¹ http://wikiserv.esrf.fr/id19/index.php/PCO_Dimax_Reconstruction:_NEW_MACROS_-_fasttomo_awerner

angle range to be reconstructed. For example, if continuous acquisition is performed with 2000 projections over 20 turns (1 scan = 1000 projections over 180°), using “standard” reconstruction numbering, scan 1 will be the one recorded between 0° and 180°, scan 2 between 180° and 360°, etc ... However, there is absolutely no restriction to use the projections acquired between 90° to 270° to reconstruct a 3D images which would corresponds to scan number “1.5”. Again, the *fasttomo_awerner* function is fully operational for this kind of reconstruction by simply using an optional argument: *fasttomo_awerner* (“num_scan”, 1.5). Using this method, successive reconstructions can be performed using overlapping group of projections. While the scan time remains the same, such method allows one to artificially reduce the temporal resolution between two successive 3D images and capture in more details the trigger of events inside the sample. Figure 33 illustrates the different outputs produced in different conditions of acquisition and reconstruction. It is clear, even if reconstruction algorithm assumptions remain unclear, that much more details can be obtained from such data treatment.

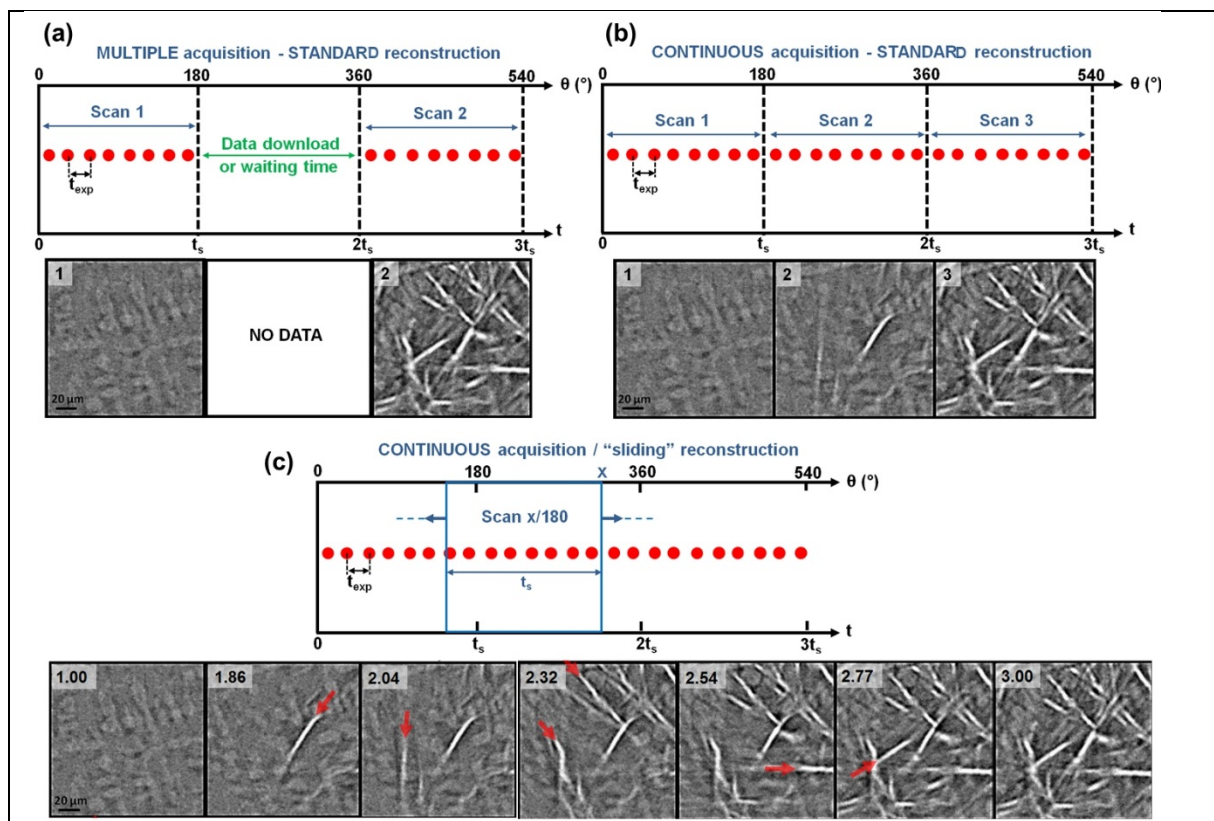


Figure 33: Comparison of produced output using (a) Multiple acquisitions containing gap between successive scans using “integer” numbering of scans (b) Continuous acquisition without gap between successive scans using “integer” numbering of scans (c) Continuous acquisition without gap between successive scans using a “sliding window” producing reconstruction of “non-integer” scans. Horizontal axes represent corresponding angular and temporal scales during acquisition of successive scans, with t_{exp} the exposure time and t_s the scan time.


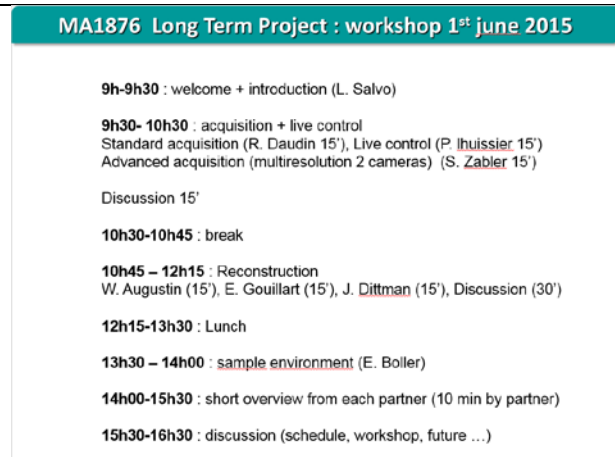
3D Data analysis (E. Guillard, SVI) : 3D image processing with sci_kit image and the scientific python system

During the user meeting 2016 E. Guillard gave a tutorial on the use of sci-kit image. The slides are located here : <https://speakerdeck.com/emmanuelle/esrf-tutorial-3-d-image-processing-with-scikit->

[image](#) and the data where those obtained during the LTP and located here https://github.com/emmanuelle/image-processing-tutorials/blob/master/tomo_segmentation.ipynb

Task 3.2 : participation and organisation of workshop

Since there are lot of members in this LTP we organized a workshop at ESRF in order to exchange on the technical and scientific results of the various partners. This workshop was held the 1st june 2015 at ESRF and exchanges were fruitfull. It allowed to have a clear view of the science performed by the various team and also presents all the technical development that have been developed. Furthermore during this workshop was finalized the technical choices for the triple-mic, designed by Optique Peter. There is a discussion among partners to organize a larger workshop in which all the researcher that use LTP work could be invited to present their results and wishes coupled with some tutorials in 3D data analysis.

	
Figure 34 : workshop annoucement	Figure 35 : workshop programme

4. List of publications and conferences directly resulting from beamtime of the LTP

Papers published :

- MIRONI, Alessandro, BRUN, Emmanuel, GOUILLART, Emmanuelle, et al. The PyHST2 hybrid distributed code for high speed tomographic reconstruction with iterative reconstruction and a priori knowledge capabilities. Nuclear Instruments and Methods in Physics Research Section B: Beam, Interactions with Materials and Atoms, 2014, vol. 324, p. 41-48.
- Ferré, A., Dancette, S., & Maire, E. (2015). Damage characterisation in aluminium matrix composites reinforced with amorphous metal inclusions. *Materials Science and Technology*, 31(5), 579-586.
- Daudin, R., Terzi, S., Lhuissier, P., Salvo, L., & Boller, E. (2015). Remelting and solidification of a 6082 Al alloy containing submicron yttria particles: 4D experimental study by in situ X-ray microtomography. *Materials & Design*, 87, 313-317.
- Bouttes, D., Gouillart, E., Boller, E., Dalmas, D., & Vandembroucq, D. (2014). Fragmentation and Limits to Dynamical Scaling in Viscous Coarsening: An Interrupted in situ X-Ray Tomographic Study. *Physical review letters*, 112(24), 245701.A

- D. Bouttes, O. Lambert, C. Claireaux, W. Woelffel, D. Dalmas, E. Gouillart, P. Lhuissier, L. Salvo, E. Boller, D. Vandembroucq (2015). Hydrodynamic coarsening in phase-separated silicate melts. *Acta Materialia*, 92, 233-242.
- K. Heim, G.S. Vinod-Kumar, F. García-Moreno, A. Rack, J. Banhart “Stabilisation of aluminium foams and films by the joint action of dispersed particles and oxide films” *Acta Materialia* 99, 313–324 (2015)
- M. Ullherr and S. Zabler, Correcting multi material artifacts from single material phase retrieved holo-tomograms with a simple 3D Fourier method, *Opt. Express* 23 (2015) 32718-32727, doi:10.1364/OE.23.032718.
- Hannard, F., Pardoën, T., Maire, E., Le Bourlot, C., Mokso, R., & Simar, A. (2016). Characterization and micromechanical modelling of microstructural heterogeneity effects on ductile fracture of 6xxx aluminium alloys. *Acta Materialia*, 103, 558-572.
- Daudin, R., Terzi, S., Lhuissier, P., Tamayo, J., Scheel, M., Babu, N. H., ... & Salvo, L. (2017). Particle-induced morphological modification of Al alloy equiaxed dendrites revealed by sub-second in situ microtomography. *Acta Materialia*, 125, 303-310.
- GOUILLART, Emmanuelle, NUNEZ-IGLESIAS, Juan, et VAN DER WALT, Stéfan., Analyzing microtomography data with Python and the scikit-image library., *Advanced Structural and Chemical Imaging*, 2017, vol. 2, no 1, p. 18.

Invited Conferences or Keynote :

- R. Daudin, D. Jauffrès, P. Lhuissier, C. Martin, L. Salvo, J. Villanova, E. Boller, S. Terzi, M. Di Michiel, M. Scheel, 4D in situ X-ray tomography in materials science, AFLS conference 16-20 november 2015, Grenoble, France.
- R. Daudin, D. Jauffrès, P. Lhuissier, J. Villanova, M. Scheel, E. Boller, S. Terzi, L. Salvo, C. Martin, 4D X-ray tomography: recent technical development and applications, 9th European Solid Mechanics Conference (ESMC 2015), July 6 - 10, 2015, Leganés-Madrid, Spain.
- R. Daudin, D. Jauffrès, P. Lhuissier, J. Villanova, M. Scheel, E. Boller, S. Terzi, L. Salvo, C. Martin, 4D in situ X-ray tomography in materials science, Mapping the Future of Materials Science (SF2M 2015), Sept 7 - 9 , 2015, Sèvres, Paris (France).
- E. Gouillart et al “In-situ tomographic imaging at high temperature”, Industrial workshop on industrial tomography, nov 2015, Antwerp
- E. Gouillart “Capturing rapid phase transformations in glass melts with 3D tomographic imaging” ESRF user meeting 09/2/2016

Conference talk

- Ani Darlapudi; Sofiane Terzi; Michelle Alvarez; Pierre Lhuissier; Luc Salvo; Elodie Boller, « Investigation of the nucleation of intermetallics in Al-Si-Fe Alloys using high speed in situ microtomography”, 3DMS conference Annecy may 2014.
- Bouttes D., Vandembroucq D., Gouillart E., Dalmas D., Boller E., Morphology of Phase Separation and Coarsening of BaO – SiO₂ – B₂O₃ by X-Ray microtomography The 8th International Conference on BORATE GLASSES, CRYSTALS AND MELTS, Paradubice, June 30 - July 14 2014

- Woelffel W., Chopinet M-H., Toplis M. J., Boller E., Gouillart E, Influence of the early melting reactivity stages on the soda-lime glass heterogeneities content., ESG Conference, Parma, 21-24 September
- Pierre Lhuissier, Mario Scheel, Robin Gibaud, Louis Marciliac, Rémi Daudin, Elodie Boller, Luc Salvo, Jean-Jacques Blandin, In situ high temperature deformation: interest of 4D characterization at higher strain rate, 3DMS conference Annecy may 2014.
- Antoine FERRE, Eric Maire, Sylvain Dancette, Damage in amorphous crystalline composite, 3DMS conference Annecy may 2014.
- E. Gouillart et al, In-situ tomographic imaging of glass batch melting at the ID19 beamline (ESRF), Euromat 2015, Warsaw
- E. Gouillart et al, Hydrodynamic coarsening in phase-separated silicate melts observed by in-situ synchrotron microtomography, Euromat 2015, Warsaw
- E. Gouillart et al, In-situ tomography of phase-separation in barium borsilicate melts, ICTMS 2015, Quebec
- E. Gouillart et al, Influence of calcium incorporation on soda-lime glass batch melting reactivity, GOMD-Acers 2015, Miami
- W. Woelffel, M. Chopinet, M. J. Toplis, E. Véron, E. Boller, E. Gouillart, Physical and chemical mechanisms happening in soda-lime batch melting followed by in situ imaging, GOMD-DGG, May 2015 (Miami, USA)
- E. Gouillart, W. Woelffel, M. Chopinet, M. J. Toplis, L. Salvo, P. Lhuissier, E. Boller, A particle-scale view of glass batch melting thanks to in situ microtomography, GOMD 2016, May 2016 (Madison, USA)
- Ferré, A., Maire, E., Dancette, S. Caractérisation de l'endommagement dans les matériaux composites amorphe/cristallin frittés au SPS. *Poudres et Matériaux Frittés 2013 22 au 24 mai 2013 Belfort.*
- Hannard, F., Simar, A., Maire, E., & Pardoën, T. (2015). Heterogeneity informed quantitative micromechanical approach of ductile fracture in 6xxx aluminium alloys. In *4th International Conference on Computational Modeling of Fracture and Failure of Materials and Structures (CFRAC 2015)*.
- Hannard, F., Simar, A., Maire, E., & Pardoën, T. (2015). Micromechanical modelling and in situ 3D microtomography characterization of microstructure heterogeneities effects on damage in aluminium alloys. In *9th European Solid Mechanics Conference (ESMC 2015)*.
- M. Paepflow, F. García-Moreno, A.J. Meagher, A. Rack, J. Banhart, Coalescence avalanches in liquid aluminium foams, MetFoam2015, 31 August-2 September 2015, Barcelona, Spain
- K. Heim, A. Ershov, F. García-Moreno, A. Rack, J. Banhart, Investigation of particle movements and drainage in liquid metallic films by synchrotron radioscopy, oral presentation at the Metfoam2015, 31 August-2 September 2015, Barcelona

PhD and Post doc directly linked to the LTP :

- David BOUTTES (<https://tel.archives-ouvertes.fr/PASTEL/tel-01078337v2>) "Micro-tomographie d'un borosilicate de baryum démixé : du mûrissement à la fragmentation", defence 8 oct. 2014.

- Antoine FERRE : “Endommagement dans les composites à matrice métallique et renfort amorphe” defence in 2015
- PhD William Woelffel using in-situ tomography as principal technique of characterization, title “Réactivité effective des mélanges vitrifiables granulaires silico-sodocalciques “ defended on 01/12/2015 December 1st. Time spent at ESRF only during experiments (June and Nov 2015). <http://www.theses.fr/2015PA066598>
- PhD F. Hannard : damage nucleation growth and coalescence in 6XXX alloys
- PhD Damien Boloré using in-situ tomography, started in December 2014
- Post Doc Rémi Daudin (EXOMET project) : nano composites and solidification
- Post doc Thérèse Bormann (EDDAM project) : amorphous bulk metallic composites